Journal of Magnetic Resonance **154,** 236–251 (2002)
doi:10.1006/jmre.2001.2463, available online at http://www.idealibrary.com on IDEAL®

Improved Narrowband Dipolar Recoupling for Homonuclear Distance Measurements in Rotating Solids

G. Goobes and S. Vega

Department of Chemical Physics, Weizmann Institute of Science, 76100 Rehovot, Israel

Received June 7, 2001; revised September 27, 2001; published online January 16, 2002

Recovery of the magnetic dipolar interaction between nuclei bearing the same gyromagnetic ratio in rotating solids can be promoted by synchronous rf irradiation. Determination of the dipolar interaction strength can serve as a tool for structural elucidation in polycrystalline powders. Spinning frequency dependent narrowband (nb) RFDR and SEDRA experiments are utilized as simple techniques for the determination of dipolar interactions between the nuclei in coupled homonuclear spin pairs. The magnetization exchange and coherence dephasing due to a fixed number of rotor-synchronously applied π-pulses is monitored at spinning frequencies in the vicinity of the rotational resonance (R^2) conditions. The powder nbRFDR and nbSEDRA decay curves of spin magnetizations and coherences, respectively, as a function of the spinning frequency can be measured and analyzed using simple rate equations providing a quantitative measure of the dipolar coupling. The effects of the phenomenological relaxation parameters in these rate equations are discussed and an improved methodology is suggested for analyzing nbRFDR data for small dipolar couplings. The distance between the labeled nuclei in the 1,3-$^{13}C_2$-hydroxybutyric acid molecule is rederived using existing nbRFDR results and the new simulation procedure. A nbSEDRA experiment has been performed successfully on a powder sample of singly labeled 1-^{13}C-L-leucine measuring the dipolar interaction between the labeled carboxyl carbon and the natural abundant β-carbon. Both narrowband techniques are employed for the determination of the nuclear distances between the side-chain carbons of leucine and its carbonyl carbon in a tripeptide Leu-Gly-Phe that is singly ^{13}C-labeled at the leucine carbonyl carbon position.

Key Words: **spinning-frequency-dependence; RFDR; SEDRA; homonuclear distance measurement; rotational resonance; magic angle spinning.**

INTRODUCTION

Utilization of the dipole–dipole interaction for the measurements of local conformation has been a primary objective of modern high-resolution solid state NMR. The dipolar interaction helps to gain insight into the organization of amorphous materials (*1*), polymers (*2*), organic solids (*3*), and biosystems (*4*). The design of new dipolar recoupling techniques that can be accomplished conveniently and that are applicable at high magnetic fields and under fast magic angle spinning (MAS) conditions is pursued continuously (*5*). NMR techniques utilizing MAS and rf irradiation sequences for the determination of dipolar coupling between homonuclear spins are constantly being refined. Traditional experiments such as R^2 (*6*), DRAMA (*7*), SEDRA (*8*), and RFDR (*9*) have been followed by improved pulse schemes such as DRAWS (*10*), MELODRAMA (*11*), CEDRA (*12*), C7 (*13*), RIL (*14*), and others (*5*). These techniques were developed to increase the efficiency at which the interaction is recoupled, reduce the influence of other interactions, and minimize pulse imperfections.

Rotating the powder samples around an axis inclined at the magic angle with respect to the external magnetic field averages out the chemical shift anisotropies and the secular dipolar interactions between spin-1/2 nuclei. In order to restore the dipolar evolution most recoupling techniques make use of rf fields that are applied synchronously with the sample spinning. These rf irradiation schemes cause a disruption of the coherent averaging and result in dipolar dephasing of spin polarizations or coherences. The decaying signals are followed as a function of the recoupling interval and are analyzed in terms of the dipolar coupling constants. The accuracy of these dipolar coupling measurements, for example between carbon nuclei, can be degraded by incomplete heteronuclear decoupling from tightly coupled protons (*15*) and by interference between the rf-fields applied on the protons and the low-abundant spins. These additional attenuation mechanisms of the time dependent signals complicate data analysis and are associated with zero-quantum (ZQ) relaxation (*16*) and other (*17*) types of relaxation processes.

Experiments that minimize these relaxation effects are of practical importance for reliable distance measurements. The idea that the spinning frequency dependence can serve as an alternative for the time dependence of the recoupling was recently suggested (*17*). Different approaches characterized by constant time experiments were introduced. The Rotational Resonance Tickling technique (*18*) employs rf-field variations sweeping through resonance criteria. The constant-time homonuclear dipolar recoupling method utilizes two RFDR periods that are varied to maintain an overall constant mixing period (*19*). The first period recouples the dipolar interaction and the second partially refocuses the dipolar evolution in a way analogous to the t-SEDRA experiment (*20*). The latter technique was used to

1090-7807/02 $35.00

study the antibody bound state of the V3 loop of the HIV-1 glycoprotein derivative (*21*).

Previously, a narrowband RFDR (nbRFDR) experiment was introduced that showed a strong spinning frequency dependence of the homonuclear dipolar recoupling efficiency (*22, 23, 17*) around the rotational resonance conditions. This spinning frequency dependence was utilized as an experimental variable for measuring dipolar interactions at a fixed mixing time (*17*). The decay of longitudinal magnetization differences was shown to be sensitive to the strength of the dipolar interaction and was employed to deduce nuclear distances. At $n = 2$ rotational resonance conditions, where the chemical shift anisotropy is larger than the spinning frequency, the orientation of the dipolar vector with respect to the CSA tensor interactions could be determined. This was used to differentiate between two crystallographic moieties in terms of torsion angles in hydroxybutyric acid. The nbRFDR approach requires only a small number of π-pulses during each experiment and can easily be implemented in any spectrometer. It can therefore be favorable over other techniques, despite its lower recoupling efficiency.

A simple model was proposed to treat various relaxation mechanisms that can interfere with the measurements, and a procedure for relieving their effect on data analysis was suggested. This procedure relied on the notion that the recoupling period of these experiments is nearly fixed. This method for the data analysis was only suitable for short distance measurements with coupling constants larger than about 200 Hz.

Here we have extended the analysis of the spinning frequency dependent nbRFDR signals to small dipolar couplings where the relaxation processes are expected to be significant. The rate equation describing the nbRFDR spin evolution has been reexamined and an improvement of the data analysis is suggested in the next section. NbSEDRA experiments are also discussed and guidelines for its application are presented. In the following section examples of nbRFDR and nbSEDRA results are shown and analyzed in terms of nuclear distances varying between 2.5 and 4.5 Å.

THE NbRFDR RATE EQUATION

Recently, we have shown (*17*) that nbRFDR experiments can be interpreted by solving a rate equation describing the evolution of the zero-quantum magnetization vector $\bar{m}$ (*6, 16*). During this magnetization exchange experiment on homonuclear pairs of nuclei with spin $I = \frac{1}{2}$, longitudinal magnetization differences are monitored as a function of the spinning frequency for a fixed number $(2N \cdot l)$ of rotor cycles containing $2l$ π-pulses with N cycles per pulse. The magnetization difference $m_z(\Omega)$ of a spin pair in a crystallite, with an orientation defined by the Euler angles $\Omega \equiv (\alpha, \beta, \gamma)$ in the rotor frame, evolves according to a nbRFDR Hamiltonian $H(\Omega; t)$. This Hamiltonian contains chemical shift and dipolar terms that are modulated by the spinning frequency and an rf term representing the π-pulses. The lowest order Magnus expansion term of this Hamiltonian in the interaction frame of the chemical shift and rf terms has the form (*22, 23*)

$$\bar{H}(\Omega) = \frac{1}{2}|d_{12}| \cos\delta_{12}(I_+^1 I_-^2 + I_+^1 I_-^2) + \frac{i}{2}|d_{12}| \times \sin\delta_{12}(I_+^1 I_-^2 - I_+^1 I_-^2). \quad [1]$$

In this frame a rotational motion of a vector $\bar{m}(\Omega; t)$ in the zero-quantum subspace can represent the effective evolution of the spins (*6, 16*). The components of this vector are proportional to the expectation values

$$\begin{aligned} m_x(\Omega; t) &= \langle I_+^1 I_-^2 + I_-^1 I_+^2 \rangle(t) \\ m_y(\Omega; t) &= \langle I_+^1 I_-^2 - I_-^1 I_+^2 \rangle(t) \\ m_z(\Omega; t) &= \langle I_z^1 - I_z^2 \rangle(t), \end{aligned} \quad [2]$$

and the Hamiltonian of Eq. [1] can be represented by an effective dipolar interaction field $d_{12}(\Omega) = |d_{12}| \exp\{i\delta_{12}\}$ in the transverse plane of the zero quantum subspace, directed at an angle δ_{12} to the x axis. For each crystallite orientation a set of polar angles $\Omega_d(\Omega) \equiv (\theta_d, \varphi_d)$ exists, relating the dipolar vector to the rotor frame at some time $t = 0$. The dipolar field nutates $\bar{m}(\Omega; t)$ around its axis. The size of the field vector varies from crystallite to crystallite and therefore the nutation frequency is different for different crystallite orientations. The total magnetization vector of the powder, $\bar{m}(t)$, decreases for an increasing time of exposure to the nbRFDR dipolar field.

In addition to this process, the $m_i(\Omega; t)$ components are also influenced by a single zero-quantum relaxation rate Γ_2^{ZQ}, when it is assumed that a single rate constant represents the transverse relaxation mechanism of all crystallites (*6, 16, 17*). Two additional relaxation parameters must be taken into account to represent the evolution of the spins. These two effective longitudinal relaxation rates $\Gamma_1^{1,2}$ reduce the expectation values of the individual z-magnetizations $\langle I_z^{1,2} \rangle$ of each pair. When they differ in magnitude the $\bar{m}(\Omega; t)$ vector becomes coupled to the longitudinal sum-magnetization, $M_z(\Omega; t) = \langle I_z^1 + I_z^2 \rangle(t)$, and a set of coupled rate equations describes the spin evolution

$$\frac{d}{dt}\begin{pmatrix} m_x \\ m_y \\ m_z \\ M_z \end{pmatrix}(\Omega; t) = \begin{pmatrix} -\Gamma_2^{ZQ} & 0 & -d_{12}^{\mathrm{Im}} & 0 \\ 0 & -\Gamma_2^{ZQ} & d_{12}^{\mathrm{Re}} & 0 \\ d_{12}^{\mathrm{Im}} & -d_{12}^{\mathrm{Re}} & -\Gamma_1^{+} & -\Gamma_1^{-} \\ 0 & 0 & -\Gamma_1^{-} & -\Gamma_1^{+} \end{pmatrix}\begin{pmatrix} m_x \\ m_y \\ m_z \\ M_z \end{pmatrix}(\Omega; t), \quad [3]$$

with $\Gamma_1^{\pm} = 1/2(\Gamma_1^1 \pm \Gamma_1^2)$ and $\bar{d}_{12}(\Omega) = d_{12}^{\mathrm{Re}} + i d_{12}^{\mathrm{Im}}$. This set

of coupled equations is an extension to the rate equations for $\bar{m}$ introduced previously by Levitt *et al.* (*6*). The relaxation rates represent a combination of experimental factors, such as the decay of the magnitudes of the magnetization components during the finite π-pulses due to cross polarization and inefficient heteronuclear proton decoupling during the pulse interval. The actual T_1 spin–lattice relaxation times of the spins are assumed to be much longer than the length of the nbRFDR recoupling period. However, they can also have some minor influence on the values of the phenomenological $\Gamma_1^{1,2}$parameters. The relative magnitude of the effective $\Gamma_1^{1,2}$ and the Γ_2^{ZQ} rates can vary significantly depending on experimental parameters.

The approximate dipolar field strength in the zero-quantum space for a coupled spin pair has been derived previously (*17, 22, 23*) and has the form

$$\bar{d}_{12}(\Omega, \omega_R) = \frac{1}{2}\sum_{n=-2}^{2} Z_n^{12} \cdot \mathrm{K}(\Delta\omega, \omega_R). \qquad [4]$$

The Z_n^{12} coefficients are conveniently reduced to the form

$$Z_{\pm n}^{12} = \omega_d^{12} \cdot G_{|n|} \exp(\pm in\varphi_d), \qquad [5a]$$

with

$$\begin{aligned} G_1 &= -\frac{3}{8}\sin(2\theta_m)\sin(2\theta_d) \\ G_2 &= -\frac{3}{8}\sin^2(\theta_m)\sin^2(\theta_d) \end{aligned} \qquad [5b]$$

for vanishing chemical shift anisotropy interactions. Full expressions can be found in a previously published work (*22*). The angle between the rotor axis and the external magnetic field, θ_m, is the magic angle given by $\tan^{-1}(\sqrt{2})$. The dipolar interaction is affecting the expressions in Eq. [5] through its strength and orientation. The strength is related to the internuclear distance vector, $\vec{r}_{12}$, by $\omega_d^{12} = -\mu_0\gamma^2\hbar/4\pi|\vec{r}_{12}|^3$ and the orientation is defined via the angles θ_d and φ_d. The dependence of the effective dipolar field on the relative magnitude of the spinning frequency ω_R with respect to the off-resonance difference $\Delta\omega$ of the spin pair is expressed by the sinc-function $\mathrm{K}(\Delta\omega, \omega_R)$

$$\mathrm{K}(\Delta\omega, \omega_R) = \mathrm{sinc}\left\{N\pi\left(n - \frac{\Delta\omega}{\omega_R}\right)\right\}, \qquad [6]$$

with $n = \pm 1, \pm 2, \ldots$. The signals that are detected during the nbRFDR experiment are proportional to the integral of $m_z(\Omega; \tau_m)$ over all crystallites at time $\tau_m = 2N\tau_R \cdot l$. Knowing the values of $\bar{d}_{12}(\Omega)$ and assuming the relaxation rates in Eq. [3], the nbRFDR signal as a function of the spinning frequency can be simulated by solving this rate equation for all crystallites.

A solution for $m_z(\Omega, \tau_m)$ can be easily evaluated, when the $\Gamma_1^{1,2}$ relaxation rates of the two spins are equal and when for simplicity we rotate the zero-quantum space so that $\bar{d}_{12}(\Omega)$ points in the x direction with a magnitude equal to $d_{12}(\Omega) = |\bar{d}_{12}(\Omega)|$. In that case Eq. [3] can be reduced to

$$\frac{d}{dt}\begin{pmatrix} m_y \\ m_z \end{pmatrix}(\Omega; t) = \begin{pmatrix} -\Gamma_2^{ZQ} & d_{12}(\Omega) \\ -d_{12}(\Omega) & -\Gamma_1^{+} \end{pmatrix}\begin{pmatrix} m_y \\ m_z \end{pmatrix}(\Omega; t) \qquad [7]$$

and can be solved as shown before (*6, 16*) for an initial condition $m_z(\Omega; 0) = 1$. A similar set of equations were recently derived by Karlsson *et al.* (*16*) using a Liouville space approach for the description and measurement of zero-quantum relaxation effects in rotational resonance experiments.

For $|d_{12}(\Omega)| > 1/2|\Gamma_2^{ZQ} - \Gamma_1^{+}|$ the solution for the longitudinal difference-magnetization is given by

$$m_z(\Omega; t) = \{\cos(\omega_{12}(\Omega)t) + \varepsilon \cdot \sin(\omega_{12}(\Omega)t)\}e^{-Rt} \qquad [8]$$

with

$$\omega_{12}(\Omega) = \sqrt{\left|(d_{12}(\Omega))^2 - \frac{1}{4}\left(\Gamma_2^{ZQ} - \Gamma_1^{+}\right)^2\right|}, \quad R = \frac{1}{2}\left(\Gamma_2^{ZQ} + \Gamma_1^{+}\right) \qquad [9]$$

and

$$\varepsilon = \frac{1/2\left(\Gamma_2^{ZQ} - \Gamma_1^{+}\right)}{\omega_{12}(\Omega)}. \qquad [10]$$

As long as the dipolar interaction is much larger than the difference between the relaxation rates and $\varepsilon \ll 1$, Eq. [8] can be approximated by

$$m_z(\Omega; t) \cong \cos(d_{12}(\Omega)t) \cdot e^{-\frac{1}{2}\left(\Gamma_2^{ZQ} + \Gamma_1^{+}\right)t}. \qquad [11]$$

For a decreasing dipolar interaction the ε-coefficient becomes significant and the solution of Eq. [7] for $|d_{12}(\Omega)| < 1/2|\Gamma_2^{ZQ} - \Gamma_1^{+}|$ becomes

$$m_z(t) = \{\cosh\omega_{12}(\Omega)t + \varepsilon \cdot \sinh\omega_{12}(\Omega)t\}e^{-Rt}. \qquad [12]$$

In this case the influence of the two relaxation parameters is different in the sense that, for $\Gamma_2^{ZQ} \cong 0$ the ε-coefficient approaches -1 and Eq. [12] becomes $m_z(\Omega; t) \cong \exp\{-(1 - (d_{12}(\Omega)/\Gamma_1^{+})^2)\Gamma_1^{+}t\}$, while for $\Gamma_1^{+} \cong 0$ we get that $\varepsilon \cong 1$ and $m_z(\Omega; t) \cong \exp\{-(d_{12}(\Omega)/\Gamma_2^{ZQ})^2\Gamma_2^{ZQ}t\}$. As expected the zero-quantum relaxation becomes undetectable for vanishing dipolar interactions, while the single quantum relaxation influences the signals even for $d_{12}(\Omega) = 0$.

The dependence of $\bar{d}_{12}(\Omega)$ on θ_d in Eq. [4] indicates that in a powder its magnitude varies between zero and about ω_d^{12}. For small $\bar{d}_{12}(\Omega)$ values, $m_z(\Omega, t)$ evolves according to Eq. [12] and for large values the time dependence of $m_z(\Omega, t)$ follows Eq. [8] or even [11]. The portion of crystallites with $m_z(\Omega, t)$

values that can not be approximated by Eq. [11] depends on the relative magnitudes of the relaxation rates and ω_d^{12}. Therefore the total nbRFDR powder signal $f_d(t)$, that corresponds to the solutions of the rate equations in Eq. [7], does not necessarily follow the expression

$$f_d(t) \cong \frac{1}{8\pi^2} e^{-Rt} \int d\Omega \cos(d_{12}(\Omega)t), \qquad [13]$$

at the rotational resonance condition for large ω_d^{12} values, as was already noted before (*15*). For some fixed time $\tau_m = 2N\tau_R \cdot l$ and with $\omega_d^{12}\tau_m \geq 2\pi$ many of the individual $\bar{m}(\Omega, t)$ vectors perform large precession angles up to $t = \tau_m$ and their z-components interfere destructively. Thus the $m_z(\Omega; \tau_m)$ values of only those crystallites that exhibit small $d_{12}(\Omega)$ values contribute constructively to the observed nbRFDR signals. At rotor frequencies far from the rotational resonance condition most crystallites are in the small $d_{12}(\Omega)$ regime and therefore are hardly dependent on Γ_2^{ZQ}.

The overall ω_R-dependent nbRFDR signal is thus dependent on Γ_2^{ZQ}, only near the resonance criterion, while Γ_1^+ influences the signal significantly everywhere. As a result, and as will be shown in the following section, the effect of zero-quantum relaxation on the powder nbRFDR curves will only be considered in cases where its rate is suspected to be significantly high. When $\omega_d^{12} > \Gamma_1^+$ again most of the crystallites evolve according to Eq. [11] and their nbRFDR signals interfere destructively, leaving the main contribution to the nbRFDR decay from small $d_{12}(\Omega)$ values. The crystallites with those $d_{12}(\Omega)$ values show a significant decay according to Eq. [12] and

$$m_z(t) \cong e^{d_{12}^2/\Gamma_1^+ t} e^{-\Gamma_1^+ t}. \qquad [14]$$

Far from rotational resonance all crystallites follow Eq. [14] and the powder signal is principally dependent on Γ_1^+:

$$f(t) \cong e^{-\Gamma_1^+ t}. \qquad [15]$$

At this point we conclude that the influence of relaxation times on the nbRFDR curves is predominantly governed by the Γ_1^+ mechanism. As we will show, the methodology of analysis suggested in Ref. (*17*) is only valid for relatively large $\omega_d^{12}/2\pi$ values with respect to the relaxation parameters.

In actual nbRFDR experiments we measure the individual signals of the two spins separately. Thus instead of the powder signal $f(t)$ two signals are measured given by

$$f_{1,2}(t) = \frac{1}{8\pi^2} \int d\Omega (M_z(\Omega, t) \pm m_z(\Omega, t)). \qquad [16]$$

With the initial conditions $m_z(\Omega, 0) = 1$, $M_z(\Omega, 0) = 0$, and $\Gamma_1^- = 0$ both signals evolve according to $f_1(t) = -f_2(t)$. This is not the case when the longitudinal relaxation times differ and $\Gamma_1^- \neq 0$. Then the rate equation in Eq. [2] cannot be reduced to Eq. [7] and the set of four coupled equations must be solved. An analytical solution for these equations can be derived; yet, it does not give more insight than numerical solutions. Examples of spin pairs that exhibit different Γ_1 values are shown in following sections.

Up to this point we have shown that the simplified expression for the nbRFDR curve in the form $f_d(\omega_R; \tau_m) = c \cdot f_d^0(\omega_R; \tau_m)$, where c represents a relaxation parameter and where $f_d^0(\omega_R; \tau_m)$ represents the relaxation-free nbRFDR decay curve, is not always sufficient to analyze experimental data. For dipolar interactions $\omega_d^{12} \gg 1/2|\Gamma_2^{ZQ} - \Gamma_1^+|$, c-coefficients can be found to fit the data around the rotational resonance conditions, as was shown previously (*17*), but they are not primarily governed by Γ_2^{ZQ}. An improved simulation procedure must therefore be suggested to calculate nbRFDR curves over the whole ω_R range and for all values of ω_d^{12}. In the next section we will do so and describe the methodology used to analyze our data.

SIMULATIONS

To quantify the effect of relaxation on the nbRFDR signals and to simulate experimental nbRFDR curves numerical calculations were performed varying the dipolar coupling and the different relaxation parameters. The expressions for $d_{12}(\Omega, \omega_R)$ given here in Eq. [4] and in Eq. [15] of Ref. (*17*), which were derived from a zero-order average Hamiltonian, and their insertion into the rate equation of Eq. [3] did not produce sufficiently accurate nbRFDR curves $f_d^0(\omega_R; \tau_m)$. Comparing single crystallite average Hamiltonian simulations with numerical simulations, using stepwise integration of the Liouville von-Neuman equation, showed discrepancies between the exact spin evolution and the zeroth order average Hamiltonian results for long mixing times. This discrepancy, originating from higher order terms, was intensified when powder averages were calculated. We therefore extracted the value $d_{12}(\Omega, \omega_R)$ for each crystallite orientation and spinning frequency from exact 4×4 density matrix calculations of $m_z^0(\Omega, \omega_R; t)$. For each set of parameters (Ω, ω_R), nbRFDR signals $m_z^0(\Omega, \omega_R; t)$ were calculated as a function of l, with $t = 2N\tau_R \cdot l$, taking into account dipolar, CSA, and rf parameters of the experiment. The main frequency component of this time dependent signal, obtained by Fourier transformation, was then set equal to $d_{12}(\Omega, \omega_R)$ and was inserted into Eq. [3]. Solving this rate equation for L different crystallite orientations as a function of ω_R and for a set of Γ_2^{ZQ} and Γ_1^+ parameters yielded the values $m_z(\Omega, \omega_R; \tau_m)$. A summation of all these values over the L discrete crystal orientations, produced the powder nbRFDR signal:

$$f(\omega_R; \tau_m) = \frac{1}{L} \sum_i m_z(\Omega_i, \omega_R; \tau_m). \qquad [17]$$

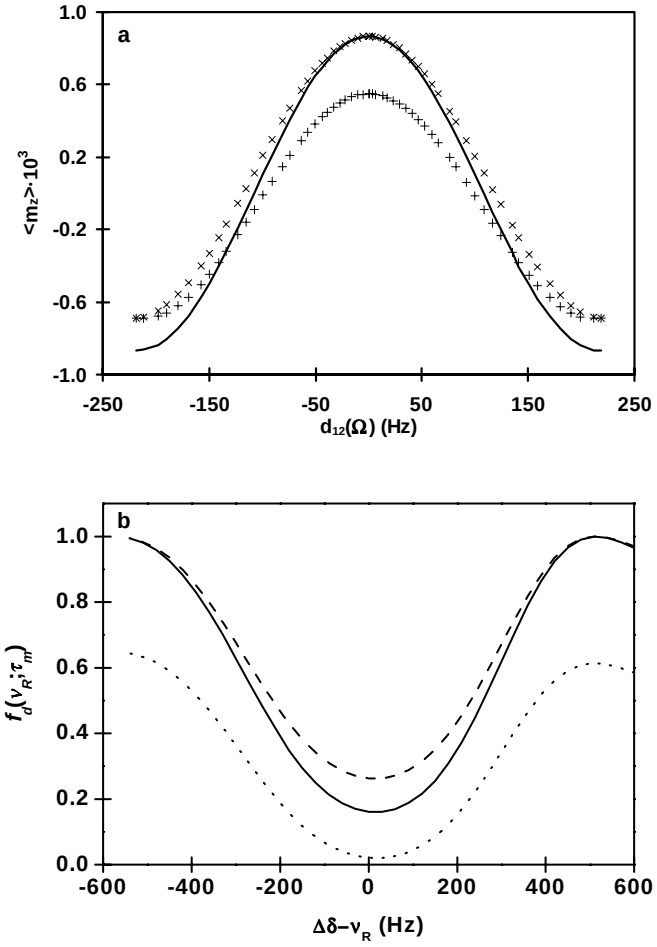

FIG. 1. (a) Individual contributions to a powder nbRFDR signal from $m_z^0(\Omega, \tau_m)$ and $m_z(\Omega, \tau_m)$ components (multiplied by 10^3) as a function of the effective dipolar coefficient $d_{12}(\Omega)$. They were calculated for a spin pair with $\nu_d = 100$ Hz and $\Delta\delta = 8750$ Hz at $\nu_R = 8800$ Hz using $\{l, N\} = \{4, 16\}$ and $\tau_m = 3.6$ ms. The solid line corresponds to $m_z^0(\Omega, \tau_m)$ calculated without relaxation; the (+) symbols correspond to $m_z(\Omega, \tau_m)$ with $\lambda_2^{ZQ} = 0$ and $\lambda_1^+ = 5$ Hz and the (×) symbols correspond to $m_z(\Omega, \tau_m)$ with $\lambda_2^{ZQ} = 5$ Hz and $\lambda_1^+ = 0$ as a function of the single crystallite $d_{12}(\Omega)$. (b) Powder nbRFDR curves of the same spin system are simulated with relaxation parameters $\{\lambda_2^{ZQ}, \lambda_1^+\}$ equal to $\{0, 0\}$ Hz (solid line), $\{5, 0\}$ Hz (dashed line), and $\{0, 5\}$ Hz (dotted line) and plotted as a function of the spinning frequency varying between 8200 and 9350 Hz.

For convenience the following frequency variables are defined in units of Hertz: $\Delta\delta = \Delta\omega/2\pi$, $\nu_d = \omega_d^{12}/2\pi$, $\nu_R = \omega_R/2\pi$, $\lambda_1^+ = \Gamma_1^+/2\pi$, $\lambda_2^{ZQ} = \Gamma_2^{ZQ}/2\pi$. In Fig. 1a, the individual $m_z^0(\Omega, \tau_m)$ and $m_z(\Omega, \tau_m)$ components evaluated at $\nu_R = 8750$ Hz close to the $n = 1$ rotational resonance condition, with $N = 16$ and $l = 4$ and at a spinning frequency $\nu_R = 8800$ Hz are shown as a function of their $d_{12}(\Omega)$ values for $\nu_d = 100$ Hz. The relaxation-free results $m_z^0(\Omega, \tau_m)$ are compared with results $m_z(\Omega, \tau_m)$ that were obtained by taking into account the relaxation parameters: (*i*) $\lambda_2^{ZQ} = 0$ and $\lambda_1^+ = 5$ Hz and (*ii*) $\lambda_2^{ZQ} = 5$ Hz and $\lambda_1^+ = 0$. The differences between these two cases are very pronounced around $d_{12}(\Omega) = 0$. The single quantum relaxation reduces the magnetization of the crystallites considerably as opposed to the ZQ mechanism that has no attenuating effect in this regime. Powder integration of these results calculated for variable ω_R gave rise to the powder nbRFDR curves in Fig. 1b that for case (i) are lower and for case (ii) are higher than the relaxation free curve. The influence of Γ_2^{ZQ} on nbRFDR curves becomes much less pronounced when ω_d^{12} increases. Thus for most of the range of observable dipolar couplings, ZQ relaxation can be ignored. We found numerically that a ZQ-relaxation rate that is 20 times smaller than the dipolar interaction results in a nbRFDR decay that deviates from the relaxation-free one by about 10%. For small interactions $\nu_d \cong 100$ Hz, a ZQ-relaxation time of 33 ms, corresponding to $\lambda_2^{ZQ} = 5$ Hz, yields a nbRFDR decay that fits relaxation-free curves of about $\{\nu_d - 10\}$ Hz, resulting in an estimated nuclear distance that deviates from its actual value by ~0.15 Å.

DATA ANALYSIS

In practice the values of the relaxation parameters are highly dependent on the experimental setup and the rf characteristics of the spectrometer. The experimental nbRFDR data, $S(\omega_R; \tau_m)$, must be fitted to calculated curves $f_d(\omega_R; \tau_m)$ that are corrected for these effective relaxation mechanisms. A possible way of data analysis, suggested in Ref. (*17*), is to multiply the experimental curves $S(\omega_R; \tau_m)$ by a constant that is equal to $c_1 = 1/c = \exp\{\Gamma_1^{eff}\tau_m\}$ and that compensates for the effect of relaxation:

$$f_d^0(\omega_R; \tau_m) = c_1 \cdot S(\omega_R, \tau_m). \qquad [18]$$

From the above discussion it follows that c_1 is mainly determined by Γ_1^+. In Fig. 2, examples of model curves $f_d(\omega_R; \tau_m) \equiv S(\omega_R; \tau_m)$ (empty circles) for (a) $\nu_d = 400$ Hz, $\lambda_1^+ = 5$ Hz and (b) $\nu_d = 100$ Hz, $\lambda_1^+ = 5$ Hz are compared with their corresponding $f_d^0(\omega_R; \tau_m)$ (solid lines) curves. For the strong dipolar case a value of $c_1 = 1.19$, with $\Gamma_1^{eff}/2\pi = 7.5$ Hz was used to generate $c_1 \cdot f_d(\omega_R; \tau_m)$ (filled circles). This correction resulted in a reasonable good fit to $f_d^0(\omega_R, \tau_m)$ around the rotational resonance condition. However, away from this condition the corrected curve deviates from the relaxation-free curve. This procedure is satisfactory for analyzing data of relatively small relaxation rates. When these rates are substantial with respect to the dipolar coupling the correction in Eq. [18] is no longer valid and it is necessary to include the Γ_1^+ and Γ_2^{ZQ} relaxation parameters explicitly.

It is thus necessary to follow a more accurate fitting procedure. This can be achieved when experimental data are measured at ω_R values far from the rotational resonance condition. There no recoupling occurs and the data are solely governed by $\exp\{-\Gamma_1^+\tau_m\}$, as given in Eq. [15], making it possible to deduce the value of Γ_1^+. This value can then be inserted in the

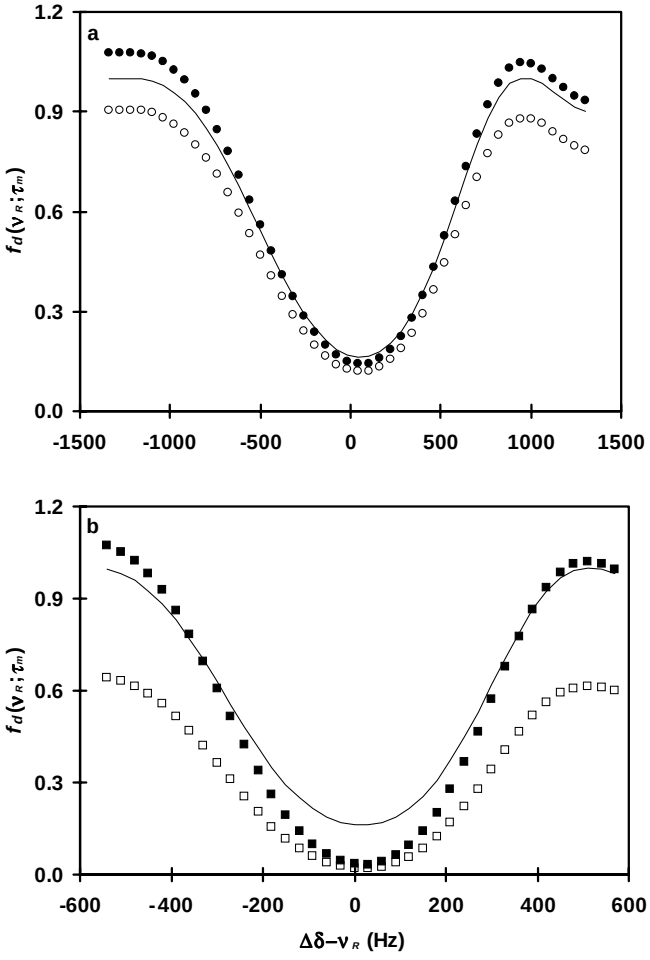

FIG. 2. Simulated nbRFDR decay curves, $f_d(\nu_R, \tau_m)$, of spin pairs with (a) $\nu_d = 400$ Hz and (b) $\nu_d = 100$ Hz and both with $\Delta\delta = 8750$ Hz, using $\{l, N\} = \{2, 8\}$ and $\{l, N\} = \{4, 16\}$, respectively. The solid lines $f_d^0(\nu_R, \tau_m)$ were simulated without taking relaxation into account. The empty symbols in both figures were evaluated with relaxation rates $\{\lambda_2^{ZQ}, \lambda_1^+\}$ equal to $\{0, 5\}$ Hz. The filled symbols are normalized nbRFDR decay curves equal to $c_1 \cdot f_d(\nu_R, \tau_m)$ (see Eq. [18]) with $c_1 = 1.19$ in (a) and $c_1 = 1.66$ in (b). As illustrated in (b) this normalization procedure fails to predict relaxation effects for small dipolar couplings.

rate equation in Eq. [3] together with the $d_{12}(\Omega, \omega_R)$ values obtained as discussed above. The resulting $f_d(\omega_R; \tau_m)$ curve must then be fitted to the experimental $S(\omega_R; \tau_m)$. When Γ_2^{ZQ} becomes significant it has to be included in the simulations as a fitting parameter, together with ω_d^{12}. When no data are available far from the rotational resonance condition, both relaxation rates must be considered as fitting parameters.

In general the initial condition of the coupled pair does not obey $S_1(\omega_R; 0) = -S_2(\omega_R; 0)$ exactly and the analysis of experimental nbRFDR data requires normalization of the initial state as discussed previously (*17*). When both spins are high abundant and both nbRFDR signals of the coupled spins are detected together with $S_1(\omega_R; 0)$ and $S_2(\omega_R; 0)$ the experimental data can be corrected according to

$$F_i(\omega_R; \tau_m) = \frac{S_i(\omega_R; \tau_m) - (1/2)(S_i(\omega_R; 0) + S_j(\omega_R; 0))}{(1/2)(S_i(\omega_R; 0) - S_j(\omega_R; 0))} \quad [19]$$

for $i, j = 1, 2$.

When one of the spins, with signal $S_1(\omega_R; \tau_m)$, is a high-abundant spin and the other is a natural-abundant spin, the nbRFDR dipolar decay is only measured on the latter spin. Its experimental function still requires that both $S_1(\omega_R; 0)$ and $S_2(\omega_R; 0)$ are detected in order to evaluate

$$F_2(\omega_R; \tau_m) = \frac{S_2(\omega_R; \tau_m) - (1/2)(S_2(\omega_R; 0) + x S_1(\omega_R; 0))}{(1/2)(S_2(\omega_R; 0) - x S_1(\omega_R; 0))} \quad [20]$$

with x the relative abundance of the low abundant spin. As long as the $F_i(\omega_R; \tau_m)$ data are available far off the rotational resonance condition we can extract the values for Γ_1^1 and Γ_1^2. These values are then used to evaluate theoretical $f_d(\omega_R; \tau_m)$ curves for different ω_d^{12} values, solving Eq. [3] and using Eq. [17]. In cases where only $F_2(\omega_R; \tau_m)$ is available we have assumed that $\Gamma_1^1 = \Gamma_1^2$. Only when the $f_i(\omega_R; \tau_m)$ curves could not be fit to $F_i(\omega_R, \tau_m)$ with $\Gamma_2^{ZQ} = 0$, did we introduce ZQ-relaxation parameters into the simulations.

SPINNING FREQUENCY DEPENDENT NbSEDRA

It is also possible to carry out narrowband SEDRA (nbSEDRA) experiments similar to the nbRFDR experiments just discussed. This experiment constitutes the same recoupling pulse sequence and therefore the same Hamiltonian as the nbRFDR experiment but involves dephasing of transverse magnetization rather then a decay of the difference-magnetization of the spin pair. Consequently, it recouples the dipolar interaction less efficiently. The nbRFDR simulations require inclusion of relaxation in rate equations describing spin dynamics, nbSEDRA simulations on the other hand require a simple multiplication of the powder calculations by a relaxation factor. Additionally, the degree of signal dephasing of each of the nuclei can be analyzed separately without knowing the coherent state of the other nucleus.

In the ideal nbRFDR case, all spin pairs are initially prepared in a state $\rho(0) = A(I_z^1 - I_z^2)$ and the density operator evolves according to the Hamiltonian given in Eq. [1] with $\delta_{12} = 0$ as

$$\rho(t) = A\left(I_z^1 - I_z^2\right)\cos(d_{12}(\Omega, \omega_R)t) + iA(I_+^1 I_-^2 - I_-^1 I_+^2) \times \sin(d_{12}(\Omega, \omega_R)t). \quad [21]$$

In nbSEDRA, the same recoupling pulse sequence is executed just after a cross-polarization excitation of the spins starting at

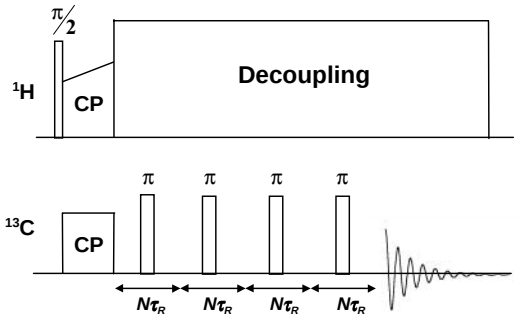

FIG. 3. The narrowband SEDRA pulse sequence: A cross polarization is followed by a set of π pulses, each pulse in the middle of a fixed period equal to a multiple number of rotor cycles $N\tau_R$. For $N = 1$ this experiment becomes a simple broadband SEDRA experiment (*8*). The signal is acquired after $2l$ pulses as a function of the spinning frequency instead of incrementing the contact period. The nbRFDR pulse sequence involves additional $\pi/2$ pulse after cross polarization, followed by a DANTE inversion interval and a delay without proton decoupling and a $\pi/2$ detection pulse after the mixing time.

a state $\rho(0) = A(I_x^1 + I_x^2)$, as shown in Fig. 3. In this nbSEDRA experiment the coherences $\langle I_x^1\rangle(\Omega, \omega_R; \tau_m)$ and $\langle I_x^2\rangle(\Omega, \omega_R; \tau_m)$ are measured as a function of the spinning frequency for a mixing time $\tau_m = l \cdot 2N\tau_R$. The effective spin evolution of the density operator yields

$$\rho(t) = A\left\{I_x^1 \cos\left(\frac{1}{2}d_{12}(\Omega)t\right) + i\left(I_z^1 I_+^2 - I_z^1 I_-^2\right) \times \sin\left(\frac{1}{2}d_{12}(\Omega)t\right)\right\} + A\left\{I_x^2 \cos\left(\frac{1}{2}d_{12}(\Omega)t\right) + i\left(I_+^1 I_z^2 - I_-^1 I_z^2\right)\sin\left(\frac{1}{2}d_{12}(\Omega)t\right)\right\}. \quad [22]$$

Just as in the nbRFDR experiment the density matrix components are exposed to relaxation mechanisms. However, since all linear spin operators in Eq. [22] are single quantum coherence operators, it is reasonable to assume that they decay according to some spin–spin relaxation times. The influence of experimental parameters will mostly manifest themselves in a shortening of these times. By assuming that the T_2-type of relaxation times are equal for all crystallites and that two relaxation parameters are sufficient to describe the nbSEDRA decays, the nbSEDRA powder signals can be written as

$$f_{1,2}(\omega_R, \tau_m) = e^{-\tau_m/T_2^{eff(1,2)}} \times \int d\Omega \left\langle I_x^{1,2}\right\rangle(\Omega, \omega_R; \tau_m) = k_{1,2} \times f_{1,2}^0(\omega_R, \tau_m). \quad [23]$$

Fitting the experimental nbSEDRA curves $S_{1,2}(\omega_R; \tau_m)$ requires a single relaxation parameter $k_{1,2}$ for each spin, in addition to ω_d^{12} and the chemical shift parameters of the spin pair, which are needed for the simulations of the $f_{1,2}^0(\omega_R; \tau_m)$ curves. Thus each nbSEDRA signal can be individually analyzed and the simulated curves can be obtained without solving rate equations similar to Eq. (3).

Examples of nbSEDRA curves $f_{1,2}^0(\omega_R; \tau_m)$ covering a dipolar coupling range of 350–600 Hz are illustrated in Fig. 4. In these calculations a chemical shift difference of $\Delta\delta = 10160$ Hz and spinning frequencies ranging between $\nu_R = 10300$–11200 Hz (Fig. 4a) and $\nu_R = 4725$–5075 Hz (Fig. 4b) were used. Similarly, in Fig. 5 nbSEDRA curves covering a coupling range of 50–300 Hz are shown for $\Delta\delta = 11100$ Hz. In these calculations the spinning frequency was varied between $\nu_R = 10550$–11050 Hz (Fig. 5a) and $\nu_R = 5275$–5525 Hz (Fig. 5b). For the larger dipolar couplings the values of (l, N) that were chosen are (2, 16) around the $n = 1$ and (2, 12) around the $n = 2$ rotational resonance criterion. Likewise, for the smaller couplings regime the

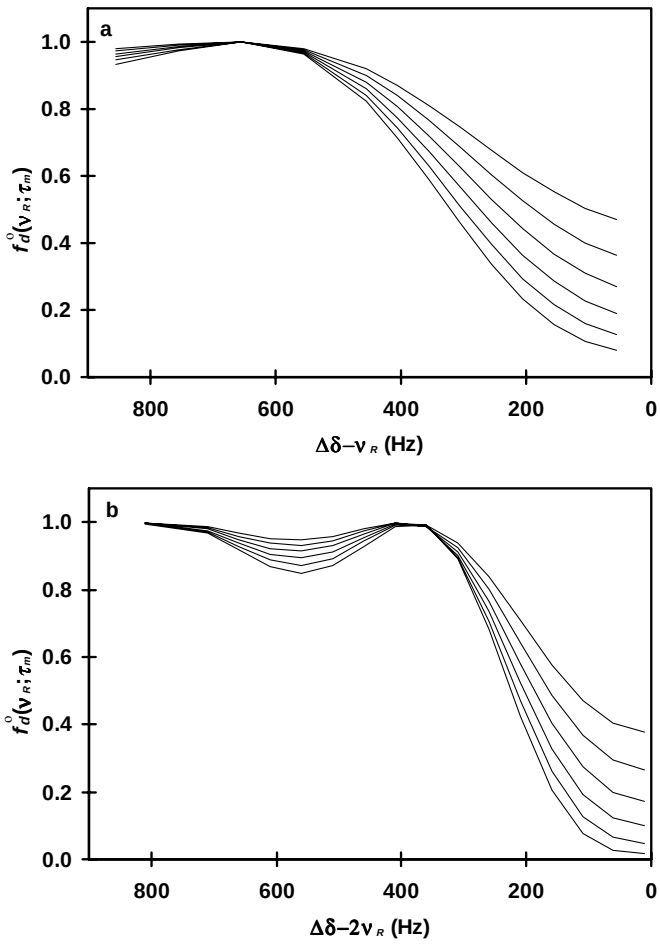

FIG. 4. Theoretical decay curves of nbSEDRA experiments on a spin pair with a dipolar coupling ranging between (top) 350 and (bottom) 600 Hz are plotted as a function of the difference between $\Delta\delta$ and the spinning frequency. In (a) simulations using $\{l, N\} = \{2, 16\}$ near the $n = 1$ R^2 condition are depicted and in (b) simulations using $\{l, N\} = \{2, 12\}$ near the $n = 2$ R^2 condition are shown. Adjacent curves in the figures have dipolar couplings that are 50 Hz apart. The isotropic chemical shift difference used in these calculations was $\Delta\delta = 10{,}160$ Hz and the CSA interactions were set to zero as well as the relaxation rate λ_2^{eff}.

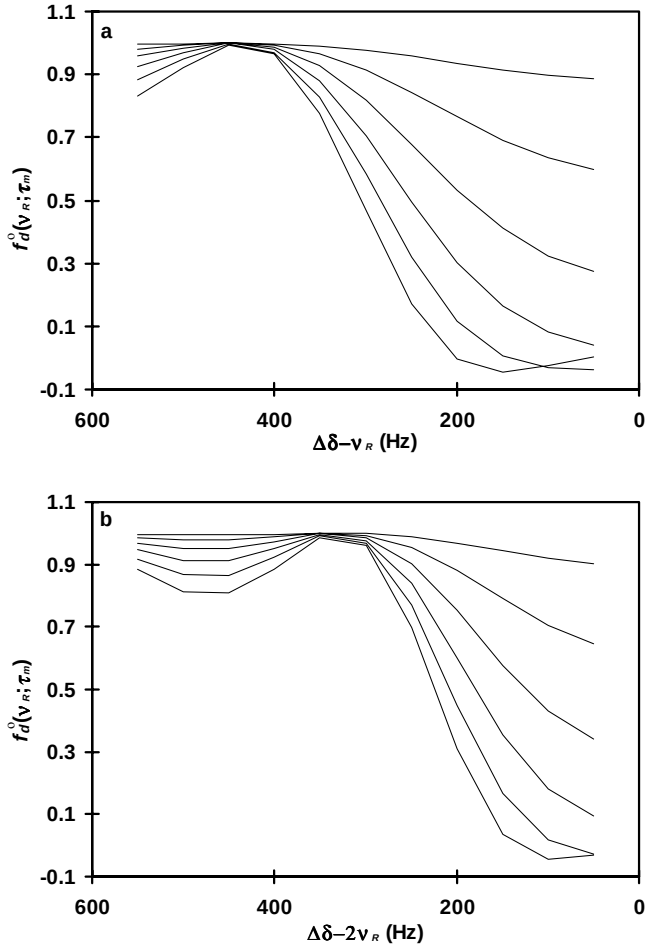

FIG. 5. Theoretical decay curves of nbSEDRA experiments on a spin pair with a dipolar coupling ranging between 50 and 300 Hz are plotted as in Fig. 4. In (a) pulse parameters $\{l, N\} = \{4, 24\}$ near the $n = 1$ R^2 condition were used and in (b) pulse parameters $\{l, N\} = \{4, 16\}$ near the $n = 2$ R^2 condition were used in the calculations. Adjacent curves in the figures have dipolar couplings that are 50 Hz apart. Neither CSA interactions nor relaxation parameters were considered.

values of (l, N) chosen are $(4, 24)$ and $(4, 16)$ for $n = 1$ and $n = 2$, respectively. When nbSEDRA signals persist for times as long as 30 ms nuclear distances up to about 5 Å can be determined.

INTERMOLECULAR DIPOLAR COUPLINGS

Additional dipolar dephasing can be promoted by interaction of the spin pair with magnetically equivalent spins on neighboring molecules. In such cases, the powder nbRFDR and nbSEDRA curves are expected to decay faster due to this intermolecular interaction. To illustrate this effect we have considered a C_a–C_b carbon spin pair with a coupling of 90 Hz, and added a supplementary $C_{b'}$ carbon that is magnetically identical to C_b at a C_a–$C_{b'}$ distance of 5.0 Å (60 Hz). NbRFDR and nbSEDRA curves $f_d^0(\omega_R; \tau_m)$ for the C_a spin were calculated using a three-spin system in the SIMPSON (*28*) program for different positions of the $C_{b'}$ carbon. The location of this carbon with respect to the C_a–C_b spin pair is defined by the polar angles $(\beta_{ab'}, \gamma_{ab'})$ of the distance vector $\bar{r}_{ab'}$ in the principal axis system of the CSA-tensor of C_a. In Fig. 6, $f_d^0(\omega_R; \tau_m)$ functions calculated for both narrowband experiments are depicted. A comparison between the C_a–C_b (solid lines) and $C_{b'}$–C_a–C_b (symbols) decay curves reveals a more pronounced effect of the third spin on the nbRFDR (top) curve than on the nbSEDRA (bottom) curve. In the nbRFDR case the additional spin would alter the best-fit parameters for $f_2^0(\omega_R; \tau_m)$ from a coupling of 90 to 120 Hz.

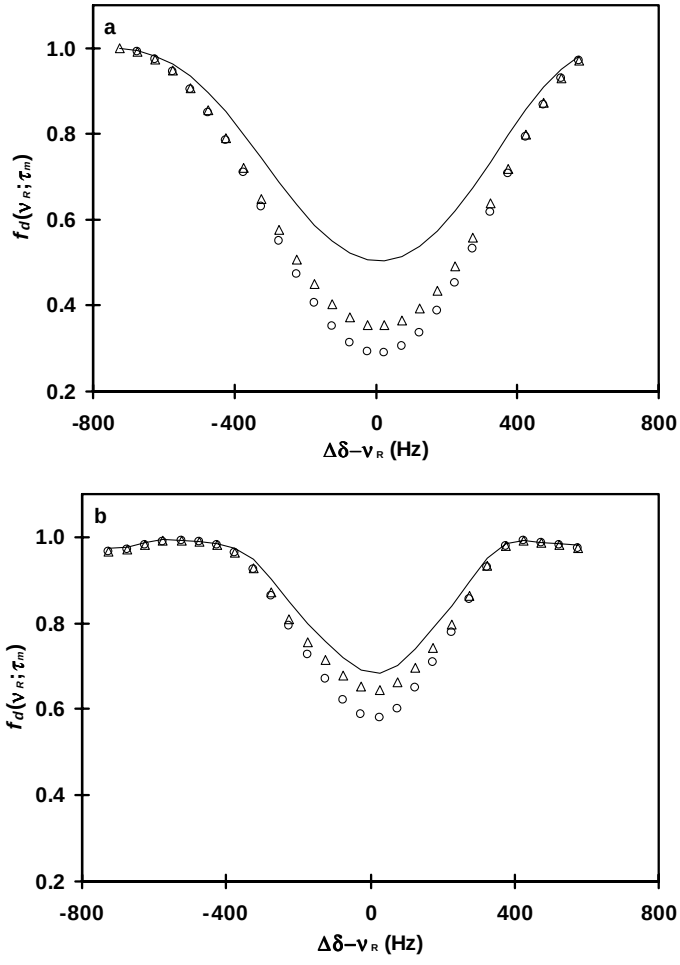

FIG. 6. The effect of intermolecular couplings on the measurement of weak dipolar couplings in nbRFDR and nbSEDRA experiments. Dipolar decay curves (solid line) of a C_a spin that is coupled by 90 Hz (4.4 Å) to a C_b spin are compared with decay curves (symbols) of the same spin that is additionally coupled by 60 Hz (5.0 Å) to an intermolecular $C_{b'}$ spin that is magnetically equivalent to C_b. NbRFDR decay curves plotted in (a) were obtained using pulse parameters $\{l, N\} = \{4, 16\}$ and nbSEDRA decay curves plotted in (b) were obtained using $\{l, N\} = \{4, 24\}$. Simulations were carried out using different polar angles $[\beta_{ab'}, \gamma_{ab'}]$ of the dipolar vector of $\bar{r}_{ab'}$ in the CSA PAS frame of C_a. Results for selected orientations with $[\beta_{ab'}, \gamma_{ab'}] = [0, 90]$ (empty circles) and $[\beta_{ab'}, \gamma_{ab'}] = [60, 90]$ (empty triangles) are depicted. The polar angle of the $\bar{r}_{ab}$ vector were $[\beta_{ab}, \gamma_{ab}] = [60, 90]$ and the C_a CSA parameters were $\omega_{CSA} =$ 5 kHz and $\eta = 0.95$ in these calculations.

SELECTIVE DANTE INVERSION

The initial state of the nbRDFR magnetization exchange experiment on a spin pair is prepared by selectively inverting one of the spins. In our case, we accomplished this with the application of a DANTE pulse sequence (*25*) on the high-abundant carboxyl or carbonyl carbons in the samples. These carbons have CSA tensors (∼75 ppm) that exhibit sidebands in their MAS spectra and that must be inverted together with their centerbands. We employed 32 equally spaced pulses of about 5.625° each during two rotor periods. Despite the large CSA parameters the selective inversion worked reasonably well. For example, to achieve optimal inversion of the carbonyl carbon in leucine at a spinning frequency in the range $\nu_R = 4$–8 kHz the length of the DANTE pulses was extended by about 5% to 5.9°. Small changes in the initial polarization at different offset values induced by the CSA parameters can be expected. This indicates that experimental optimization is necessary to obtain efficient inversion and that an accurate detection of the $S_{1,2}(\omega_R; 0)$ signals must be carried out in conjunction with the $S_{1,2}(\omega_R; \tau_m)$ measurements.

MATERIALS AND EXPERIMENTAL METHODS

DL-3-Hydroxybutyric acid (HBA) 1,3-$^{13}C_2$ sodium salt was purchased from Isotec Inc. (Matheson–Trigas, Miamisburg, OH). A polycrystalline sample of L-[1-^{13}C,^{15}N]-leucine was purchased from Cambridge Isotope Labs (Andover, MA). In this sample the leucine molecules are labeled at the carboxyl carbons and the amine nitrogen. A selectively labeled peptide Leu-Gly-Phe (LGF) was synthesized by Dr. Ingolf Sack (*26*). This molecule was synthesized manually by an Fmoc strategy, using L-[1-^{13}C,^{15}N]-leucine, [2, 2-d_2]-glycine and L-[^{15}N]-phenylalanine. The isotopes were enriched by 98% at least. Experiments on all samples were carried out on a Bruker DSX300 spectrometer equipped with a 4-mm double-tuned WB MAS probe. The nbSEDRA pulse scheme is shown in Fig. 3 and the nbRFDR pulse scheme was given elsewhere (*17*). The rf field exerted on the protons during the $\pi/2$ pulse was 90 kHz. During the cross polarization (CP) period the field was ramped from 43 to 86 kHz. During the TPPM decoupling period and throughout the rest of the experiment the field was 92.5 kHz. Efficient CP was attained using a ^{13}C-irradiation field of 65 kHz with a contact time of 1 ms for the leucine sample, 4 ms for the LGF sample, and 2 ms for the HBA sample. Carbon dipolar recoupling was achieved using π pulses of 90 kHz. The nbRFDR experiments included an additional $\pi/2$ flip-back pulse of 2.7 μs, a selective DANTE inversion sequence followed by a coherence dephasing period of 8 rotor periods without proton decoupling, and a $\pi/2$ detection pulse again of 2.7 μs, as explained previously (*17*). The DANTE inversion scheme was composed of 32 pulses of 0.29 μs at a power level of 65 kHz applied over an interval of $2\tau_R$. Experiments on the leucine sample were performed at spinning frequencies of 10,450–11,000 Hz near the $n = 1$ condition and at spinning frequencies of 4800–5500 Hz near the $n = 2$ condition. Similarly, nbRFDR and nbSEDRA experiments on the tripeptide were conducted at spinning frequencies varying in the 11,550–10,800 and 11,200–10,100 Hz ranges, respectively. Spinning frequencies were stabilized to within ±1 Hz. The π-pulses on the carbons were phase-cycled according to the XY-4 and XY-8 phase cycling schemes (*27*).

Simulations of the nbRFDR and nbSEDRA experiments were carried out using the SIMPSON simulation package for solid state NMR (*28*) considering all CSA parameters, dipolar coupling parameters, isotropic chemical shifts and pulse lengths, phases, and amplitudes. A short Matlab (*29*) program was written to calculate single crystallite and powder signals stemming from the rate equations presented in Eq. [3]. This program diagonalizes the relaxation matrix of the rate equation and calculates $m_z(\Omega, \omega_R; \tau_m)$ and $f_{1,2}(\omega_R, \tau_m)$. The CSA values of the leucine carboxyl carbon reported before (*30*) were used and were confirmed in a slow spinning CPMAS experiment.

RESULTS AND DISCUSSION

NbRFDR Measurements of Hydroxybutyric Acid

In Ref. (*17*) we discussed the analysis of nbRFDR experiments on the two high abundant carbon nuclei in 1,3-$^{13}C_2$-hydroxybutyric acid (HBA). The ^{13}C MAS spectrum (see insert in Fig. 7a) of this molecule contained two *C–OH* lines, (1) at 64.1 ppm and (2) at 61.5 ppm, and a *COOH* line at 180.0 ppm. It was shown that the hydroxyl carbon lines correspond to two conformations of the HBA molecule in the powder sample and that the nuclear distance between the two abundant carbons is the same in both types. The analysis of the nbRFDR data, obtained around the $n = 1$ rotational resonance (R^2) condition with $(N, l) = (8, 2)$ and $\tau_m = 3.7 - 4.0$ ms, resulted in a carbon distance of 2.5 ± 0.1 Å. The approach undertaken in (*17*) to analyze the data has been extended as discussed above and as demonstrated here. For that purpose the experimental nbRFDR function, $F_{COOH}(\nu_R; \tau_m)$ of the *COOH* line and $F_{C-OH}(\nu_R; \tau_m)$ of the *C–OH* lines were rederived. The latter function is given by the average of the individual normalized F-curves of the two *C–OH* lines

$$F_{C-OH}(\nu_R; \tau_m) = \frac{1}{2}\sum_{i=1,2} \frac{S^{(i)}_{C-OH}(\nu_R; \tau_m) - (1/2)\left(S^{(i)}_{C-OH}(\nu_R; 0) + (1/2)S_{COOH}(\nu_R; 0)\right)}{(1/2)\left(S^{(i)}_{C-OH}(\nu_R; 0) - (1/2)S_{COOH}(\nu_R; 0)\right)},$$

and $F_{COOH}(\nu_R; \tau_m)$ is normalized according to

$$F_{COOH}(\nu_R; \tau_m) = \sum_{i=1,2} \frac{S_{COOH}(\nu_R; \tau_m) - ((1/2)S_{COOH}(\nu_R; 0) + S^{(i)}_{C-OH}(\nu_R; 0))}{(1/2)S_{COOH}(\nu_R; 0) - S^{(i)}_{C-OH}(\nu_R; 0)}.$$

These experimental values are plotted in Fig. 7a as a function of $\overline{\Delta\delta} - \nu_R$, where $\overline{\Delta\delta}$ is the difference between the *COOH* line

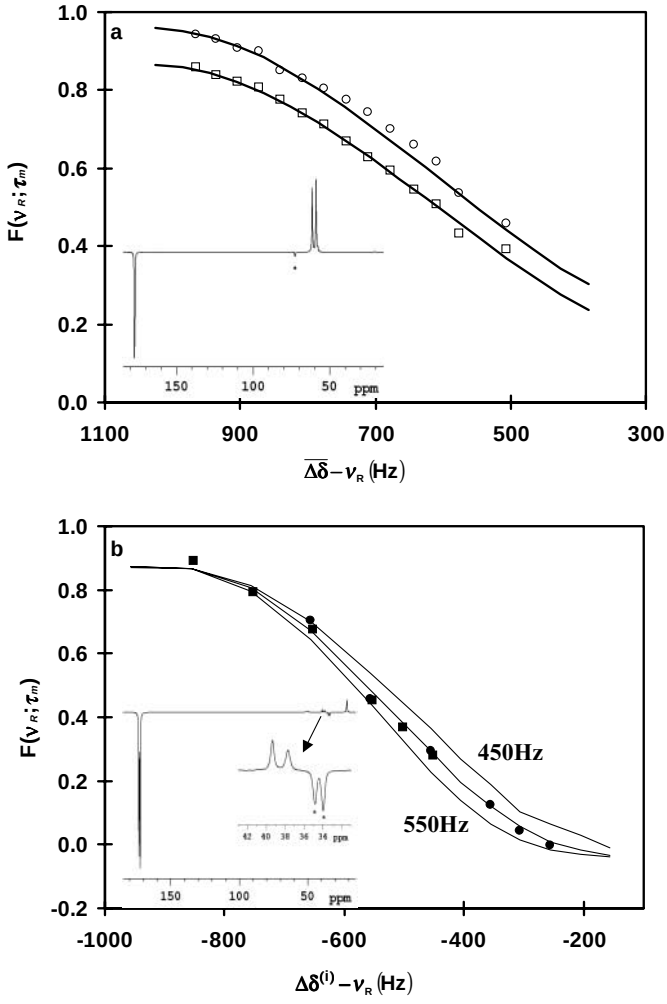

FIG. 7. (a) Experimental nbRFDR $F(\nu_R;\tau_m)$ values using $\{N, l\} = \{8, 2\}$ near the $n = 1$ R^2 condition of the (empty squares) carboxyl carbon and (empty circles) hydroxyl carbon in the HBA molecule are compared with simulated $f_d(\nu_R, \tau_m)$ curves using parameters $(\nu_d, \lambda_1^+, \lambda_1^-, \lambda_2^{ZQ})$ equal to (500, 3, 2, 0) Hz. The ^{13}C CPMAS spectrum of HBA after the selective inversion of the carboxyl carbon spectrum is shown in the insert. The carbonyl sidebands are marked with a star. (b) Experimental nbRFDR results near the $n = 1$ R^2 condition of the two C_β lines in leucine using $\{l, N\} = \{2, 12\}$. The $C_\beta^{(1)}$ data at (circles) 37.6 ppm and the $C_\beta^{(2)}$ data at (squares) 39.3 ppm are plotted each with respect to its own $\Delta\delta^{(i)}$ value with $i = 1, 2$. The simulated curves (solid lines) were obtained using $\nu_d = 450$, 500, 550 Hz and $(\lambda_1^+, \lambda_2^{ZQ})$ equal to (5, 0) Hz. The CPMAS spectrum of leucine after the selective inversion of the carboxyl carbon spectrum is shown in the insert.

position and the average line position of the *C–OH* carbons. These results are fitted to the simulated curves $f_d(\nu_R;\tau_m) = (1/2)(f_d^{(1)}(\nu_R;\tau_m) + f_d^{(2)}(\nu_R;\tau_m))$ for the *C–OH* and the *COOH* carbons. It is clearly seen from the data in this figure that the two $F(\nu_R;\tau_m)$ curves differ significantly and therefore different values for λ_1^1 and λ_1^2 must be considered in the relaxation model. Thus to fit the data $\lambda_1^{C-OH} = 2.5$ Hz, corresponding to a relaxation time of 64 ms, and $\lambda_1^{COOH} = 0.5$ Hz, corresponding to a relaxation time of 318 ms, were used. These values were deduced from the measurement at an off-R^2 frequency of $\nu_R = 7.8$ kHz. With these λ_1 values and $\lambda_2^{ZQ} = 0$, the $f(\nu_R;\tau_m)$ curves (solid lines) using $\nu_d = 500$ Hz exhibit the best agreement with the experimental data. This analysis resulted in an accurate determination of an internuclear distance of 2.48 ± 0.05 Å that is in agreement with the known distance of 2.48 Å obtained from X-ray diffraction data (*31*). Not only did the rate equation model allow a good prediction of the nbRFDR dipolar decay over the whole range of spinning frequencies, it also increased the accuracy of the nuclear distance measurement.

NbRFDR and NbSEDRA Measurements of Leucine

To show the feasibility of measuring nuclear distances between a high abundant ^{13}C and its neighboring natural abundant carbons (*32*) nbRFDR and nbSEDRA experiments were performed on a polycrystalline L-[1-^{13}C,^{15}N]-leucine sample. The ^{13}C spectrum following a DANTE inversion (see insert in Fig. 7b) of this sample shows two inverted lines (at 173.3 and 172.3 ppm) of the high abundant carboxyl carbon (C_{OOH}), one α-carbon (C_α) line (at 49.8 ppm) and two β-carbon (C_β) lines (at 39.3 and 37.6 ppm). Additionally, it shows a line composed of the overlapping γ-carbon (C_γ) and δ-carbons ($C_{\delta 1,\delta 2}$) at 21.3 ppm. This spectrum indicates that there are two conformations (1), (2) for the same molecule in the sample. NbRFDR experiments were carried out near the $n = 1$ rotational resonance condition using $\{l, N\} = \{2, 12\}$ and the signals $S_\beta(\nu_R, \tau_m)$ of the natural abundance C_β lines were collected. The assignment of the two coupled C_{OOH}–C_β spin pairs was achieved by comparing the relative intensities of the lines and confirmed by plotting the $F_\beta(\nu_R;\tau_m)$ curves of the two C_β lines as a function of $\Delta\delta - \nu_R$, for the two possible values of $\Delta\delta$ of each line.

The experimental nbRFDR function $F_\beta(\nu_R;\tau_m)$, with $x = 0.01$ in Eq. [20], for the two sites is shown in Fig. 7b as a function of $\Delta\delta^{(i)} - \nu_R$, with $i = 1, 2$. The results suggest that the two types of molecules generate a common nbRFDR curve, indicating that they posses the same C_{OOH}–C_β distance. The less shielded carboxyl resonance $C_{OOH}^{(1)}$ is coupled to the more shielded β-carbon $C_\beta^{(1)}$, and the more shielded carboxyl-carbon $C_{OOH}^{(2)}$ is coupled to the less shielded β-carbon $C_\beta^{(2)}$. The isotropic shift differences of the two pairs are $\Delta\delta^{(1)} = 135.7$ ppm and $\Delta\delta^{(2)} = 133$ ppm. The simulated data, using a dipolar interaction of 500 Hz ($r = 2.48$ Å) and a relaxation parameter $\lambda^+ = 5$ Hz produced a good fit to the experimental data with an accuracy of the dipolar coupling that is ±50 Hz (±0.08 Å). No ZQ-relaxation was used in these calculations.

NbSEDRA data in the vicinity of the $n = 1$ and the $n = 2$ rotational resonance conditions, with $\{l, N\} = \{2, 16\}$ and $\{l, N\} = \{2, 12\}$, respectively, were also acquired. The line intensities of the C_β signals were divided by the corresponding signal intensities detected immediately after proton–carbon cross-polarization to give the normalized experimental nbSEDRA function $G(\omega_R;\tau_m)$. The data far from the rotational resonance condition were used to estimate the $T_2^{eff(i)}$ values. The simulated $f_\beta^0(\omega_R;\tau_m)$ curve, for ν_d equal to 475 ± 15 Hz,

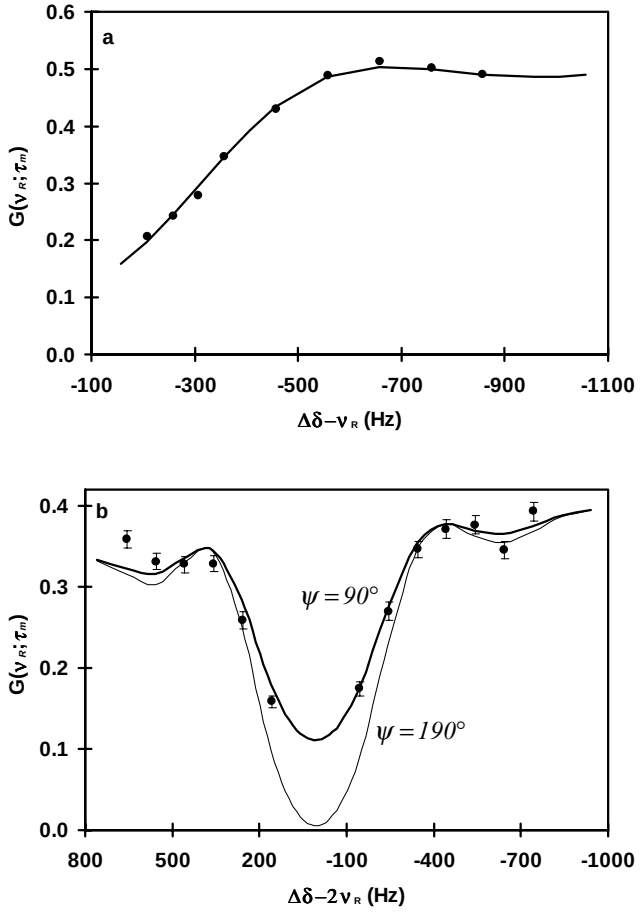

FIG. 8. NbSEDRA experiments on the $C_\beta^{(1)}$ carbon (circles) in leucine were acquired with $\{l, N\} = \{2, 16\}$ close to the $n = 1$ R^2 condition and with $\{l, N\} = \{2, 12\}$ close to the $n = 2$ R^2 condition and are plotted in (a) and (b), respectively. In (a) the simulated nbSEDRA curve (solid line), obtained by using $\nu_d = 475$ Hz and $k^{(1)} = 0.56$, is fitted to the experimental data, $G(\nu_R; \tau_m)$. In (b) simulations using $\nu_d = 475$ Hz and $k^{(1)} = 0.45$ are fitted to the experimental results by varying the torsion angle $0 \le \Psi \le 2\pi$ between the C_β–C_α and the $C_{OOH} = O$ bonds. Only the maximal (thin line) nbSEDRA curve with $\psi = 90°$ and the minimal (thick line) nbSEDRA curve with $\psi = 190°$ are shown.

was multiplied by factors $k_{(i)} = \exp(-\tau_m / T_2^{eff(i)})$, with $T_2^{eff(1)} = 10.4$ ms and $T_2^{eff(2)} = 8.65$ ms. The resulting $f_d^{(i)}(\omega_R; \tau)$ curves fit the experimental data quite well as shown in Figs. 8a and 9a. The obtained coupling strength corresponds to an internuclear distance of $r = 2.52 \pm 0.03$ Å that agrees well with the nbRFDR measurements and the distance deduced from previous X-ray diffraction work (*33*).

The nbSEDRA data and their fitted simulations near the $n = 2$ condition are shown in Figs. 8b and 9b. In the evaluation of the $d_{12}(\Omega, \omega_r)$ coefficients the principal values of the carboxyl CSA tensor were taken into account, while those of the β-carbon were small enough to be neglected. The principal axes system (PAS) of the CSA tensor was chosen according to a previous study (*34*) with its z axis perpendicular to the sp^2 plane of the carboxyl group and its y axis in the direction of the C_{OOH}–C_α bond. The position of the β-carbon was defined by the torsion angle Ψ between the C_β–C_α bond and the $C_{OOH} = O$ double bond. This angle determines the polar angles (θ_d, φ_d) of the C_{OOH}–C_β vector in the CSA PAS of the C_{OOH} carbon. NbSEDRA data are plotted together with the $k^{(i)} f_d^0(\omega_R; \tau_m)$ curves for $\nu_d = 475$ Hz in Figs. 8b and 9b using $T_2^{eff(1)} = 11.8$ ms and $T_2^{eff(2)} = 9.3$ ms, respectively. In the simulations the torsion angle was varied and a range of curves were obtained. The minimal dephasing curve was obtained for $\Psi = 90°$ and the maximal dephasing curve was obtained for $\Psi = 190°$. The extreme dephasing curves were selected from calculations varying $0 \le \Psi \le 360$ in $\pm 10°$ steps. The simulations using $\Psi \cong 90(\pm 15)°$ describe best the experimental data for both C_β species. The value for this torsion angle derived from previous

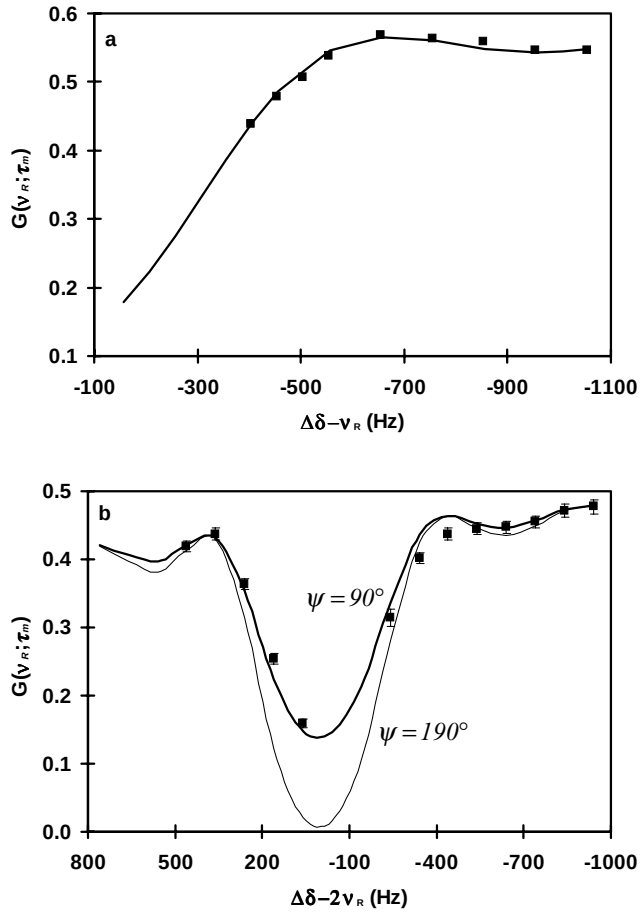

FIG. 9. NbSEDRA experiments on the $C_\beta^{(2)}$ (squares) in leucine were acquired with $\{l, N\} = \{2, 16\}$ close to the $n = 1$ R^2 condition and with $\{l, N\} = \{2, 12\}$ close to the $n = 2$ R^2 condition and are plotted in (a) and (b), respectively. In (a) the simulated nbSEDRA curve (solid line), obtained by using $\nu_d = 475$ Hz and $k^{(2)} = 0.50$, is fitted to the experimental data, $G(\nu_R; \tau_m)$. In (b) simulations using $\nu_d = 475$ Hz and multiplied by $k^{(2)} = 0.36$ are fitted to the experimental results by varying the torsion angle $0 \le \Psi \le 2\pi$ between the C_β–C_α and the $C_{OOH} = O$ bonds. Only the maximal (thin line) nbSEDRA curve with $\psi = 90°$ and minimal (thick line) nbSEDRA curve with $\psi = 190°$ are shown.

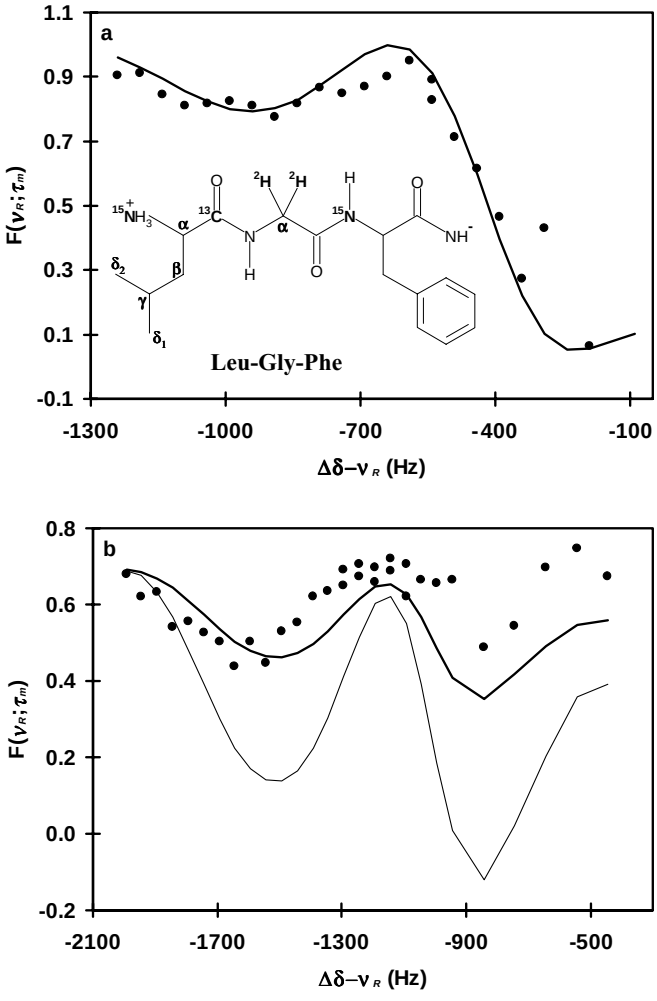

FIG. 10. In (a) are plotted the experimental nbRFDR $F(\omega_R;\tau_m)$ data of the glycine C^G_α carbon (symbols) in the singly ^{13}C-labeled LGF peptide that were acquired with $\{l, N\} = \{2, 16\}$ near the $n = 1$ R^2 condition. A simulated curve (solid line) obtained by using $(\nu_d, \lambda_1^+, \lambda_2^{ZQ})$ equal to (500, 0, 0) Hz is also shown. The primary structure of the tripeptide is shown as an insert. In (b) experimental nbRFDR $F(\omega_R;\tau_m)$ data of the leucine C^L_α carbon (symbols) in the tripeptide acquired also with $\{l, N\} = \{2, 16\}$ near the $n = 1$ R^2 condition are plotted. Simulated curves using $(\nu_d, \lambda_1^+, \lambda_2^{ZQ})$ equal to (1790, 10, 0) Hz (thin line) and (1790, 10, 100) Hz (thick line) are also shown.

crystallographic studies (*33*) is 90(±4)°, depending on the specific study.

The two C_β conformers have distinguishable isotropic chemical shifts yet this is not manifested by Ψ torsion angle differences. Presumably these differences are determined by conformation changes at the γ- and δ-carbon positions. The positions of these side-chain carbons could not be determined by nbSEDRA experiments, because they exhibit overlapping lines in the CPMAS spectrum.

NbRFDR and NbSEDRA Measurements of LGF

Both nbRFDR and nbSEDRA experiments were performed on an LGF sample (see insert in Fig. 10a), ^{13}C enriched only at the carbonyl position of the leucine, in order to detect the interaction magnitudes between this abundant carbon and the natural abundant α, β, γ, and δ-carbons $C^L_{\alpha-\delta}$ of leucine and the α-carbon C^G_α of glycine. In the analysis of the data the effective relaxation rate, λ_1^2, of the enriched carbon was taken equal to that of the interacting carbon, thus $\lambda_1^- = 0$ for all cases. The γ-carbon and the δ-carbons of the leucine residue are well resolved in the CPMAS NMR spectrum of the peptide, permitting an analysis of its side-chain structure. The less-shielded and the more-shielded δ-carbons are denoted by $C^L_{\delta(1)}$ and $C^L_{\delta(2)}$, respectively.

Measurements on Adjacent Carbons

NbRFDR results aimed at measuring the distance between the labeled carbonyl carbon and the adjacent carbons are shown in Figs. 10 and 11. The pulse parameters $\{l, N\} = \{2, 16\}$ were

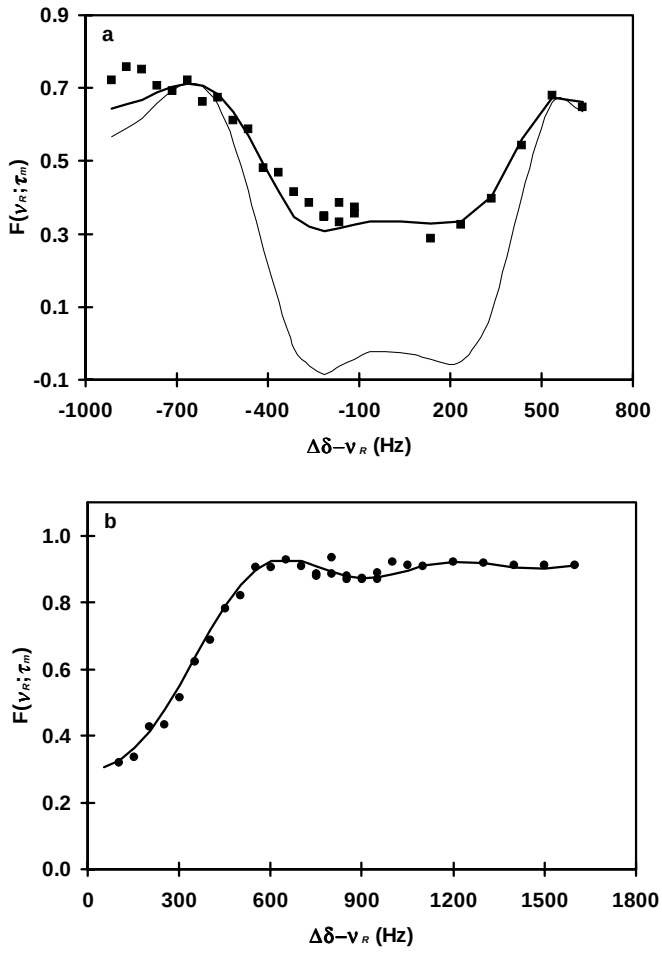

FIG. 11. In (a) experimental nbRFDR $F(\omega_R;\tau_m)$ data of the leucine C^L_β carbon (symbols) in the LGF peptide carried out with $\{l, N\} = \{2, 16\}$ near the $n = 1$ R^2 condition are shown together with simulated curves using $(\nu_d, \lambda_1^+, \lambda_2^{ZQ})$ equal to (thin line) (500, 9, 0) Hz and (thick line) (500, 9, 70) Hz. In (b) experimental nbRFDR $F(\omega_R;\tau_m)$ data of the leucine C^L_γ carbon (symbols) in the LGF peptide carried out with $\{l, N\} = \{2, 16\}$ near the $n = 1$ R^2 condition are drawn together with a simulated curve using $(\nu_d, \lambda_1^+, \lambda_2^{ZQ})$ equal to (210, 1.5, 0) Hz.

used for a wide range of spinning frequencies. The decay curves of the C_α^G and C_α^L are shown in Fig. 10. The $F(\nu_R;\tau_m)$ data points and the $f_d(\nu_R;\tau_m)$ curves with ν_d equal to 500 and 1790 Hz and λ_1^+ equal to 0 and 10 Hz, respectively, are depicted. In the case of C_α^G the calculated curve is in good agreement with the experimental data. However, for C_α^L an introduction of a large λ_2^{ZQ} value was essential to fit the experiments. A λ_2^{ZQ} value of 100 Hz was necessary to obtain a satisfactory fit. Signal to noise dispersion did not allow a better analysis. The same nbRFDR experiments were also performed on the C_β^L and C_γ^L carbons. Their $F(\nu_R;\tau_m)$ results are plotted in Fig. 11. Relaxation parameters, λ_1^+, were initially deduced from far off-R^2 measurements. Then best fittings were obtained for $(\nu_d, \lambda_1^+, \lambda_2^{ZQ})$ values equal to (500; 9; 70) Hz for the C_β^L carbon and (210; 1.5; 0) Hz for the C_γ^L carbon, corresponding to distances of 2.5 and 3.3 Å, respectively. A large value of λ_2^{ZQ} was necessary to fit the data of the β-carbon.

Measurements on Sidechain Carbons

To follow the nbRFDR signals of the C_γ^L, $C_{\delta(1)}^L$ and $C_{\delta(2)}^L$ carbons the experimental parameters were changed to $\{l, N\} = \{4, 16\}$. Figures 12b, 13b, and 14b show the nbRFDR results $F(\nu_R;\tau_m)$ of the C_γ^L, $C_{\delta(1)}^L$, and $C_{\delta(2)}^L$ carbons, respectively. The best-fit $f_d(\nu_R;\tau_m)$ curves were calculated for $(\nu_d, \lambda_1^+, \lambda_2^{ZQ})$ values of (200, 1.5, 0), (125, 0, 0), and (150, 0, 0) Hz for the C_γ^L, $C_{\delta(1)}^L$, and $C_{\delta(2)}^L$ carbons, respectively. Because no data far off the R^2 condition are available in this measurement, the λ_1^+ values had to be estimated during the curve fitting. However, it was found that the $F(\omega_R;\tau_m)$ curves of the $C_{\delta(1)}^L$ and $C_{\delta(2)}^L$ carbons could be fitted without the use of this relaxation parameter. The fitting procedure gave rise to ν_d values of 125($\pm$5) Hz for the $C_{\delta(1)}^L$ and 150($\pm$10) Hz for the $C_{\delta(2)}^L$ carbons. The C_γ^L carbon calculations resulted in ν_d value of 200($\pm$15) Hz. Experimental errors are within the size of the symbols shown in the figures.

NbSEDRA experiments were also carried out on the LGF peptide with $\{l, N\} = \{4, 24\}$ at spinning frequencies in the vicinity of the $^{13}C_{OOH}^L$–C_γ^L and the $^{13}C_{OOH}^L$–$C_{\delta(1),(2)}^L$ isotropic chemical shifts differences. These values were chosen to detect weak interactions, as shown in Fig. 5. The measured signals for the C_γ^L, $C_{\delta(1)}^L$ and $C_{\delta(2)}^L$ carbons are shown in Figs. 12a, 13a, and 14a, respectively, together with the $k \cdot f_d^0(\omega_R;\tau_m)$ curves. As before, the k values were estimated from far off-R^2 measurements. The (ν_d, k) parameters used for the fitting are (200 Hz, 2.6) for C_γ^L, (100Hz, 1.53) for $C_{\delta(1)}^L$, and (125Hz, 1.28) for $C_{\delta(2)}^L$. NbSEDRA measurements on $C_\alpha^{L,G}$ and C_β^L carbons could not be analyzed because their effective spin–spin relaxation times were very short and signals fully decayed during the mixing period.

Discussion of the LGF Measurements

Distinctively fast effective relaxation rates were found in the nbRFDR measurements on the $C_{\alpha,\beta}^L$ carbons. The C_{OOH}–C_γ^L dipolar couplings measured both by nbSEDRA and nbRFDR are similar and correspond to a distance of 3.3($\pm$0.1) Å . The C_{OOH}–$C_{\delta(1)}^L$ and C_{OOH}–$C_{\delta(2)}^L$ dipolar couplings deduced from the nbSEDRA data correspond to distances of 4.24($\pm$0.20) and 3.93($\pm$0.15) Å, respectively. A comparison of the two experiments shows that the C_{OOH}–$C_{\delta(i)}^L$ coupling constants extracted from the nbRFDR measurement do not match the couplings deduced from the nbSEDRA measurements. Moreover, the former couplings would correspond to short C_{OOH}–$C_{\delta(1)}^L$ and C_{OOH}–$C_{\delta(2)}^L$ distances, 3.9($\pm$0.2) and 3.7($\pm$0.15) Å respectively, implying a high-energy structure with the leucine sidechain bent toward the peptide backbone. Within the limitations of our relaxation model, involving the $\Gamma_1^{+,-}$, Γ_2^{ZQ}, and T_2^{eff} parameters, these discrepancies could not be explained. Moreover, variation of the leucine sidechain torsion angles could not produce a conformation that agrees with these distance measurements.

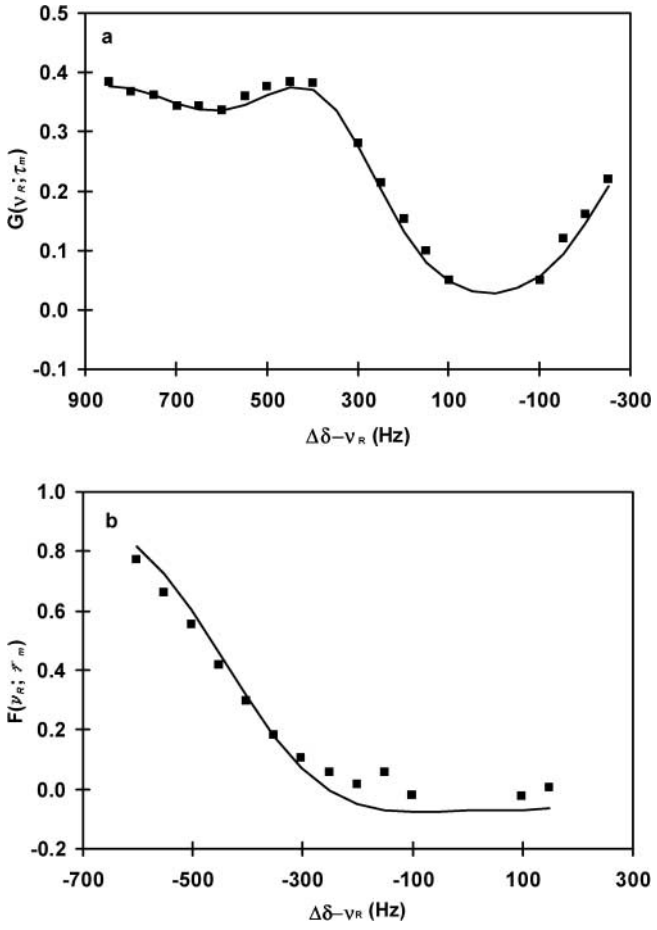

FIG. 12. In (a) nbSEDRA experimental data, $G(\omega_R;\tau_m)$, of the leucine C_γ^L carbon in LGF using $\{l, N\} = \{4, 16\}$ are shown together with a simulated curve (solid line) using $\nu_d = 200$ Hz and $k = 2.6$. In (b) nbRFDR experimental data, $F(\omega_R;\tau_m)$, of the same carbon using $\{l, N\} = \{4, 24\}$ are shown together with a simulated curve (solid line) using $(\nu_d, \lambda_1^+, \lambda_2^{ZQ})$ equal to (200, 1.5, 0) Hz. Both experiments were carried out near the $n = 1$ R^2 condition.

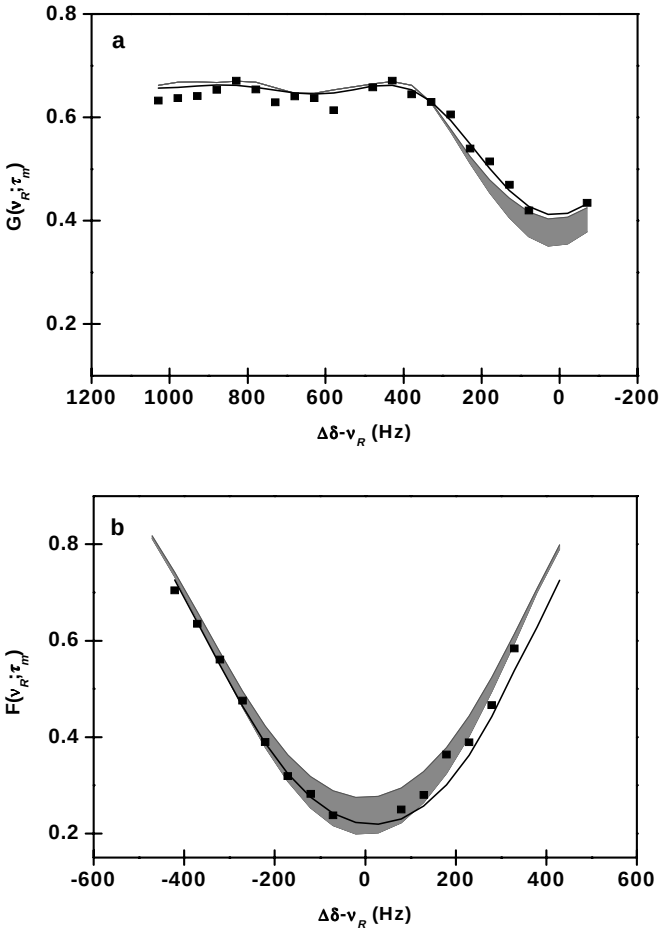

FIG. 13. NbSEDRA experiments using $\{l, N\} = \{4, 24\}$ and nbRFDR experiments using $\{l, N\} = \{4, 16\}$ carried out near the $n = 1$ R^2 condition. In (a) $G(\omega_R; \tau_m)$ data of the $C^L_{\delta(1)}$ carbon in LGF (symbols) are shown together with a simulated curve using $\nu_d = 100$ Hz and $k = 1.53$. In (b) nbRFDR data, $F(\omega_R; \tau_m)$, of the same carbon are shown together with a simulated curve (solid line) using $(\nu_d, \lambda_1^+, \lambda_2^{ZQ})$ equal to (125, 0, 0) Hz. Simulations of $C^L_{\delta(1)}$ decay curves using $(\nu_d, \lambda_1^+, \lambda_2^{ZQ})$ equal to (100, 0, 0) Hz and taking into account an additional intermolecular C^L_{OOH} carbon with a fixed dipolar interaction of 60 Hz to the $C_{\delta(i)}$ carbons and a varying position are shown as a gray band of decay curves.

A possible reason for the enhanced decay of the nbRFDR curves could be the presence of an additional abundant carbonyl carbon, $C^{(2)}_{OOH}$, on an adjacent molecule that is in close proximity to the $C^L_{\delta(i)}$ carbons to affect the data. As shown in Fig. 6, this would lower the nbRFDR curves. The resultant dipolar decay curve depends on the orientation of the $C^L_{\delta(i)}$–$C^{(2)}_{OOH}$ polar vector with respect to the $C^L_{\delta(i)}$–$C^{(1)}_{OOH}$ vector. To simulate that effect on the nbRFDR and nbSEDRA curves the additional carbonyl carbon was placed at a distance of 5 Å (60 Hz) from the $C^L_{\delta(i)}$ carbons. In the simulations, the interactions in the original spin pairs were taken to be 100 and 125 Hz for the $C^L_{\delta(1)}$ and $C^L_{\delta(2)}$, respectively. The angles between the two vectors, connecting the carbonyl carbons and the $\delta^{(i)}$-carbon, were freely varied to produce a range of decay curves. The results of these simulations are shown in Figs. 11b and 12b. It is clearly seen in these figures that the dipolar decay curves measured by both nbSEDRA and nbRFDR lie within the range of simulated curves and that the results found by the two techniques are in good agreement. The nbRFDR and nbSEDRA measurements on the side-chain carbons are summarized in Table 1. The distances extracted from these experiments are comparable to the leucine side-chain distances in the Leu-Gly-Gly (LGG) peptide as reported in previous X-ray diffraction study (*35*).

The relaxation parameters necessary for the data fitting vary from experiment to experiment and from carbon to carbon. Zero-quantum rates were necessary to fit the nbRFDR results of C^L_α and C^L_β only. NbSEDRA on both of these carbons could not

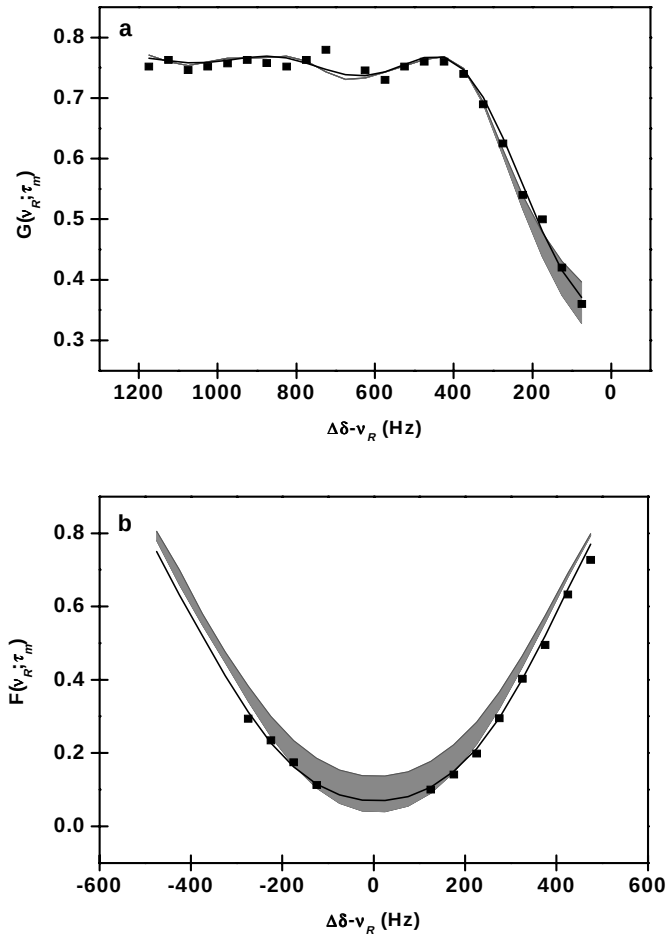

FIG. 14. NbSEDRA experiments in the LGF peptide carried out near the $n = 1$ R^2 condition using $\{l, N\} = \{4, 24\}$. In (a) experimental $G(\omega_R; \tau_m)$ data of the $C^L_{\delta(2)}$ carbon in LGF (symbols) are shown together with a simulated curve using $\nu_d = 125$ Hz and $k = 1.28$. In (b) nbRFDR data, $F(\omega_R; \tau_m)$, of the same carbon are shown together with a simulated curve (solid line) using $(\nu_d, \lambda_1^+, \lambda_2^{ZQ})$ equal to (150, 0, 0) Hz. Simulations of $C^L_{\delta(2)}$ decay curves using $(\nu_d, \lambda_1^+, \lambda_2^{ZQ})$ equal to (125, 0, 0) Hz and taking into account an additional intermolecular C^L_{OOH} carbon with a fixed dipolar interaction of 60 Hz to the $C_{\delta(i)}$ carbons and a varying position are shown as a gray band of decay curves.

TABLE 1
Molecular Distances of Leucine Sidechain in the LGF Peptide Derived from NbRFDR and NbSEDRA Experiments

	C_{OOH}–C^L_{γ}	C_{OOH}–$C^L_{\delta(1)}$	C_{OOH}–$C^L_{\delta(2)}$
NbRFDR	3.3(±0.1) Å	4.2(±0.2) Å [3.9 Å][a]	3.9(±0.2) Å [3.7 Å][a]
NbSEDRA	3.3(±0.1) Å	4.3(±0.2) Å [4.2 Å][a]	3.9(±0.2) Å [3.9 Å][a]
X-ray LGG[b]	3.3 Å	4.3 Å	3.9 Å

[a] Distances were deduced from a model taking into account an intermolecular Co carbon at a distance of 5 Å from the $C_{\delta(i)}$ carbons. Distances given in brackets were deduced from calculations neglecting this additional coupling.

[b] Data for LGG were derived from work by Goswami *et al.* (*35*).

be performed because of short effective transverse relaxation times. These two observations are perhaps connected and some relaxation mechanism, such as a fast molecular reorientation or a strong proton–carbon interaction, reduces the phenomenological relaxation rates significantly. To study the origin of these effects, temperature dependent studies could be considered. All other carbons exhibit λ_1^+ values varying between 0 and 10 Hz, with the large values, 9–10 Hz, for the $C^L_{\alpha,\beta}$ carbons, respectively, and smaller value, 1.5 Hz, for the C^L_{γ} carbon. The values of the nbSEDRA T_2^{eff} relaxation times of the γ- and the two δ-carbons are 18.7, 42.1, and 72.5 ms, respectively. The fact that the two relaxation times of the methyl carbons differ by ~30 ms is not yet understood.

CONCLUSIONS

In this publication we have shown that the nbRFDR and nbSEDRA techniques can easily be used for nuclear distance measurements between homonuclear spins. The fitting procedure suggested here has made it possible to improve the extent and the quality of distance measurements and to analyze data on spin pairs characterized by different effective longitudinal relaxation rates. The simplicity of these experiments and the straightforward data analysis can make these experiments favorable over other distance measurements, despite their inferior dephasing characteristics. Another practical aspect of the narrowband measurements is their ease with which distances between high and low abundant carbons can be determined. Because of the small span of spinning frequencies used in these experiments, effects of rf imperfections have been reduced significantly and can be accounted for by the phenomenological relaxation parameters Γ_1^+ and T_2^{eff} for a nearly constant dephasing time τ_m. As a result it can become easier to analyze narrowband experimental data rather than time dependent measurements. NbRFDR measurements are shown to be more sensitive than nbSEDRA measurements to effects of additional dipolar couplings to proximate intermolecular magnetically equivalent carbons. The narrowband techniques were employed to study the orientation of the leucine residue in the LGF peptide. Interestingly, these measurements have shown (see Table 1) that the leucine sidechain in this sample is oriented in a conformation that is similar to the leucine sidechain conformation in the LGG peptide. This is the case despite the presence of a large moiety such as the phenyl ring in the LGF molecule. Extensions of the narrowband approach toward two-dimensional homonuclear correlation and experiments in large coupled spin systems should now be considered.

ACKNOWLEDGMENT

This research was supported by the German–Israeli Foundation.

REFERENCES

1. T. M. Alam and D. P. Lang, *Chem. Phys. Lett.* **336**(5–6), 385–391 (2001); J. C. C. Chan, M. Bertmer, and H. Eckert, *J. Am. Chem. Soc.* **121,** 5238–5248 (1999); M. S. De Paul, M. Ernst, J. S. Shore, J. F. Stebbins, and A. Pines, *J. Phys. Chem. B* **101,** 3240–3249 (1997); K. Herzog, B. Thomas, D. Sprenger, and C. Jager, *J. Noncryst. Solids* **190**(3), 296–300 (1995).
2. I. Schnell, A. Watts, and H. W. Spiess *J. Magn. Reson.* **149,** 90–102 (2001); K. Saalwachter, R. Graf, D. E. Demco, and H. W. Spiess, *J. Magn. Reson.* **139,** 287–301 (1999); M. Schneider, L. Gasper, D. E. Demco, and B. Blumich, *J. Chem. Phys.* **111,** 402–415 (1999); M. G. Dunbar, D. Sandstrom, and K. Schmidt-Rohr, *Macromolecules* **33,** 6017–6022 (2000); K. Schmidt-Rohr, *J. Am. Chem. Soc.* **118,** 7601–7603 (1996).
3. D. Rovnyak, M. Baldus, B. A. Itin, M. Bennati, A. Stevens, and R. G. Griffin, *J. Phys. Chem. B* **104**(42), 9817–9822 (2000); J. H. Wu, C. D. Xiao, A. F. Yee, J. M. Goetz, and J. Schaefer, *Macromolecules* **33**(18), 6849–6852 (2000); M. T. Zell, B. E. Padden, D. J. W. Grant, M. C. Chapeau, I. Prakash, and E. J. Munson, *J. Am. Chem. Soc.* **121,** 1372–1378 (1999).
4. X. L. Yao, K. Schmidt-Rohr, and M. Hong *J. Magn. Reson.* **149,** 139–143 (2001); H. J. M. de Groot, *Curr. Opin. Struct. Biol.* **10,** 593–600 (2000); A. McDermott, T. Polenova, A. Bockmann, K. W. Zilm, E. K. Paulsen, R. W. Martin, and G. T. Montelione, *J. Biomolecular NMR* **16,** 209–219 (2000); S. O. Smith, K. Aschheim, and M. Groesbeek, *Q. Rev. Biophys.* **29,** 395–449 (1996); B. Bechinger, R. Kinder, M. Helmle, T. C. B. Vogt, U. Harzer, and S. Schinzel, *Biopolymers* **51,** 174–190 (1999).
5. S. Dusold and A. Sebald, *Ann. Rep. NMR Spectrosc.* **41,** 185–264 (2000); A. E. Bennett, R. G. Griffin, and S. Vega, *NMR Basic Princ. Prog. Chem. Phys.* **33,** 1–77 (1994).
6. M. H. Levitt, D. P. Raleigh, F. Creuzet, and R. G. Griffin, *J. Chem. Phys.* **92,** 6347–6364 (1990); D. P. Raleigh, F. Creuzet, S. K. Das Gupta, M. H. Levitt, and R. G. Griffin, *J. Am. Chem. Soc.* **111,** 4502–4503 (1989).
7. R. Tycko and G. Dabbagh, *Chem. Phys. Lett.* **173,** 461–465 (1990).
8. T. Gullion and S. Vega, *Chem. Phys. Lett.* **194,** 423–428 (1992); O. Weintraub, S. Vega, C. Hoelger, and H. H. Limbach, *J. Magn. Reson. Ser. A* **109,** 14–25 (1994).
9. A. E. Bennett, J. H. Ok, R. G. Griffin, and S. Vega, *J. Chem. Phys.* **96,** 8624–8627 (1992).
10. D. M. Gregory, D. J. Mitchell, J. A. Stringer, S. Kiihne, J. C. Shiels, J. Callahan, M. A. Mehta, and G. P. Drobny, *Chem. Phys. Lett.* **246,** 654–663 (1995).
11. B. Q. Sun, P. R. Costa, D. A. Kocisko, P. T. Lansbury, Jr., and R. G. Griffin, *J. Chem. Phys.* **102,** 702–707 (1995).
12. W. L. Zhu, C. A. Klug, and J. Schaefer, *J. Magn. Reson. Ser. A* **108,** 121–123 (1994).
13. Y. K. Lee, N. D. Kurur, M. Helmle, O. G. Johannessen, N. C. Nielsen, and M. H. Levitt, *Chem. Phys. Lett.* **242,** 304–309 (1995).

14. M. Baldus, M. Tomaselli, B. H. Meier, and R. R. Ernst, *Chem. Phys. Lett.* **230,** 329–336 (1994).
15. M. Helmle, Y. K. Lee, P. J. E. Verdegem, X. Feng, T. Karlsson, J. Legtenburg, H. J. M. de Groot, and M. H. Levitt, *J. Magn. Reson.* **140**(2), 379–403 (1999).
16. A. Kubo and C. A. McDowell, *J. Chem. Soc., Faraday Trans.* **84,** 3713–3730 (1988); T. Karlsson and M. H. Levitt, *J. Chem. Phys.* **109**(13), 5493–5507 (1998).
17. G. Goobes, G. J. Boender, and S. Vega, *J. Magn. Reson.* **146,** 204–219 (2000).
18. P. R. Costa, B. Sun, and R. G. Griffin, *J. Am. Chem. Soc.* **119,** 10821–10830 (1997).
19. A. E. Bennett, D. P. Weliky, and R. Tycko, *J. Am. Chem. Soc.* **120,** 4897–4898 (1998).
20. O. Weintraub, S. Vega, C. Hoelger, and H. H. Limbach, *J. Magn. Reson. Ser. A* **110,** 12–18 (1994).
21. D. P. Weliky, A. E. Bennett, A. Zvi, J. Anglister, P. J. Steinbach, and R. Tycko, *Nat. Struct. Biol.* **6,** 141–145 (1999).
22. G. J. Boender, Ph.D. thesis, Leiden Univ., The Netherlands, 1996; G. J. Boender, S. Vega, and H. J. M. de Groot, *J. Chem. Phys.* **112,** 1096–1106 (2000).
23. A. E. Bennett, C. M. Rienstra, J. M. Griffiths, W. Zhen, P. T. Lansbury, Jr., and R. G. Griffin, *J. Chem. Phys.* **108**(22), 9463–9479 (1998).
24. S. R. Kiihne, K. B. Geahigan, N. A. Oyler, H. Zebroski, M. A. Mehta, and G. P. Drobny, *J. Chem. Phys. A* **103,** 3890–3903 (1999).
25. G. A. Morris and R. Freeman, *J. Magn. Reson.* **29,** 433–462 (1978).
26. I. Sack, Y. S. Balazs, S. Rahimipour, and S. Vega, *J. Am. Chem. Soc.* **122,** 12,263–12,269 (2000).
27. T. Gullion, D. B. Baker, and M. S. Conradi, *J. Magn. Reson.* **89,** 479–484 (1990).
28. M. Bak, J. T. Rasmussen, and N. C. Nielsen, *J. Magn. Reson.* **147**(2), 296–330 (2000).
29. Mathworks Inc., "MATLAB 5" (version 2), 1998.
30. CH. Ye, RQ. Fu, JZ. Hu, L. Hou, and S. W. Ding, *Magn. Reson. Chem.* **31,** 699–704 (1993).
31. L. A. Aslanov, V. M. Ionov, V. A. Tafeenko, and A. N. Kost, *Zh. Strukt. Khim.* **17,** 748–749 (1976).
32. C. A. Klug, W. L. Zhu, K. Tasaki, and J. Schaefer, *Macromolecules* **30**(6), 1734–1740 (1997); I. Sack, S. Macholl, J. H. Fuhrhop, and G. Buntkowsky, *Phys. Chem. Chem. Phys.* **2**(8), 1781–1788 (2000).
33. C. H. Gorbitz and B. Dalhus, *Acta Crystallogr., Sect. C: Cryst. Struct. Commun.* **52,** 1754–1756 (1996); M. Coll, X. Solans, M. Font-Altaba, and J. A. Subirana, *Acta Crystallogr., Sect. C: Cryst. Struct. Commun.* **42,** 599–601 (1986); M. M. Harding and R. M. Howieson, *Acta Crystallogr., Sect. B: Struct. Sci.* **32,** 633–634 (1976).
34. N. Janes, S. Ganapathy, and E. Oldfield, *J. Magn. Reson.* **54,** 111–121 (1983).
35. K. N. Goswami, V. S. Yadava, and V. M. Padmanabhan, *Acta Crystallogr., Sect. B: Struct. Sci.* **33,** 1280–1283 (1977).